TITANIUM SILICALITE-1 MACROSTRUCTURES FOR USE IN PHOTOCATALYTIC REMOVAL OF ORGANIC POLLUTANTS FROM AQUEOUS MEDIA

Sean Patrick Dennis Ormond

September 2015

A thesis submitted in fulfilment of the requirements of the Manchester Metropolitan University for the degree of Master of Science by Research.

School of Science and the Environment

Faculty of Science and Engineering

Manchester Metropolitan University

ACKNOWLEDGEMENTS

First and foremost I would like to thank my supervisor, Dr. Lubomira Tosheva, for all her guidance and support over the course of my research. I am truly grateful for the opportunity to work under her tutelage. I would also like to thank my other supervisor, Professor Peter Kelly. Also to be thanked is Dr. Michele Edge, whose expertise and advice helped me during my research. A massive thank-you is owed to the lab technicians at Manchester Metropolitan University, whose instruction and advice aided me in my work.

Finally, I would like to thank my family and friends for all their support in my endeavours.

ABSTRACT

Commercial photocatalyst are in the form of nanopowders, causing aggregation, separation issues and loss of material upon regeneration. This work aims at developing free-flowing photocatalysts in the form of macroscopic beads, which are easily recoverable from solutions.

In this study, hierarchically porous TS-1 macroscopic beads were prepared via the resin templating method. Characterisation of the beads was carried out using the following methods: XRD, Raman, nitrogen adsorption/desorption, SEM and EDX. Ti content of the beads was varied in the range of 1 to 7 wt.%, with corresponding surface areas of the beads produced ranging from 725 to 350 $m^2 g^{-1}$. The beads were comprised of a large amount of amorphous material, which was required in order to achieve a high level of mechanical stability in the beads. Evaluation of the photocatalytic activity of the TS-1 beads was carried out via first order degradation kinetics of MB dye under UV irradiation. MB concentrations during the photocatalytic process were determined by UV-vis spectroscopy. CristalACTiV™ PC500, a commercially available nano-anatase photocatalyst, was used as a reference material. The TS-1 beads displayed similar rates of MB degradation independent of the Ti content, but the rates of degradation were 1.2 to 1.5 times lower than CristalACTiV™ PC500. The macroscopic shape of the TS-1 beads allows for easy separation by decanting from exhausted MB solutions after UV irradiation and reuse in subsequent cycles of photocatalytic testing. Regeneration of the catalyst was not required and no appreciable loss of photocatalytic activity was observed in up to five cycles.

CONTENTS

LIST OF ABBREVIATIONS

This page contains a list of the abbreviations and acronyms used in this body of work and their definitions.

Abbreviation	Definition
BET	Brunauer-Emmett-Teller
BDDT	Brunauer, Deming, Deming and Teller
BJH	Barrett-Joyner-Halenda
EDX	Energy-dispersive X-ray
IZA	International Zeolite Association
MB	Methylene Blue
SEM	Scanning Electron Microscopy
TEOS	Tetraethoxysilane
TEOT	Tetraethoxytitanate
TPAOH	Tetrapropylammonium hydroxide
TS-1	Titanium Silicalite-1
UV	Ultraviolet
XRD	X-ray Diffraction

1 INTRODUCTION

Destruction and pollution of the environment are serious issues currently faced by humanity. Failure to acknowledge and fix the damage to the planet will result in catastrophic consequences which will be irreversible. Research into renewable energy sources and green chemistry is therefore imperative to maintaining the habitability of the planet. Photocatalysis presents us with an opportunity to harness the clean and near infinite energy of the Sun. Through the use of photocatalytically active materials, potentially harmful pollutants can be decomposed into easier to manage products. In this work, zeolite-based materials were prepared and used for the photocatalytic decomposition of organic pollutants in an aqueous medium.

1.1 ZEOLITES

Zeolites are crystalline microporous aluminosilicates whose lattice structure define channels and cavities of regular size in the micropore size range (<2 nm).[1] These pores determine the high surface areas of zeolites, typically exceeding 400 m^2/g. Dimensions and geometry of the pores and internal voids vary depending on the lattice structure of the zeolite.[2] Based on the number of framework O or T atoms (where T = Si or Al), defining the pores, zeolites can be classified as small-pore (8 member ring), medium-pore (10 member ring) or large-pore (12 member ring) zeolites. The pore size of zeolites is comparable to the size of many molecules allowing them to act as molecular sieves, discriminating and separating mixtures based on molecular size and shape. Materials with zeolitic structures containing other elements than Si and Al have also been prepared. Examples are the titanium silicates (e.g., TS-1) and the aluminium phosphates.

The three dimensional framework of zeolites is composed of $[AlO_4]^{5-}$ and $[SiO_4]^{4-}$ tetrahedra, linked by shared oxygen atoms. For each Al atom present in the zeolite framework, a non-framework cation must be present to balance the net negative charge of the framework. The chemical composition of zeolites may therefore be expressed by the following empirical formula;[3]

$$M_{2/n}O : Al_2O_3 : xSiO_2 : yH_2O$$

where M is the counterion, n is the counterion valency, x is the SiO_2/Al_2O_3 ratio and y is the water content of the zeolite framework. Non-framework cations are generally group I or II ions, although organic, non-metal and metal cations may be used to balance charge.[4] These charge-balancing cations can be reversibly exchanged for other cations, which determine the ion-exchange properties of zeolites. Zeolites in an H-form display Brønsted acidity, which is utilised in catalytic applications. Zeolites are classified according to their framework structure with a three-letter code assigned by the International Zeolite Association (IZA), which is not related to their chemical composition and derived from the name of the type material from which the topology was confirmed. The mnemonic codes define the network of the corner sharing tetrahedrally coordinated framework atom. For example, the materials prepared in this study are MFI-type zeolites. MFI topology code is derived from Zeolite Socony **M**obil - **Fi**ve (ZSM-5). The MFI-type framework is discussed in more detail in Section 1.2.

Owing to their high surface areas, ion-exchange and catalytic properties, zeolites have found use in a wide range of applications; from water softening and water purification to molecular sieve adsorbents. In catalysis, zeolites are used in the petroleum

industry in fluid catalytic cracking processes. In addition, many emerging applications of zeolites have been reported in recent years.[5,6]

Zeolites are typically synthesized by hydrothermal treatment of reactive aluminosilicate gels or solutions in an alkaline environment. Zeolites crystallise in the form of microcrystalline powder, which needs further processing for a number of applications. Binders such as clays or amorphous silica are used to mix with the zeolite to form zeolite aggregates such as pellets and tablets of high mechanical strength. However, the use of binders can greatly reduce the performance of the zeolite due to blocking of the micropores, preventing diffusion of products and reactants to active sites. This has determined the interest in developing zeolite materials in alternative forms such as films or zeolite self-bonded macrostructures, that do not require the addition of binders.[7]

1.2 TITANIUM SILICALITE-1 (TS-1)

First synthesised in 1983 by Taramasso *et al*., titanium silicalite-1 (TS-1) is an MFI-type (Fig. 1) zeolitic compound.[8] The MFI-type structure has a three dimensional pore system, which consists of sinusoidal and straight 10-member ring channels of sizes 5.1 × 5.5 Å and 5.3 × 5.5 Å respectively, thereby making TS-1 a medium-pore zeolite. Examples of other MFI-type zeolites include silicalite-1 and ZSM-5, which are composed of silica and silica-alumina species respectively.

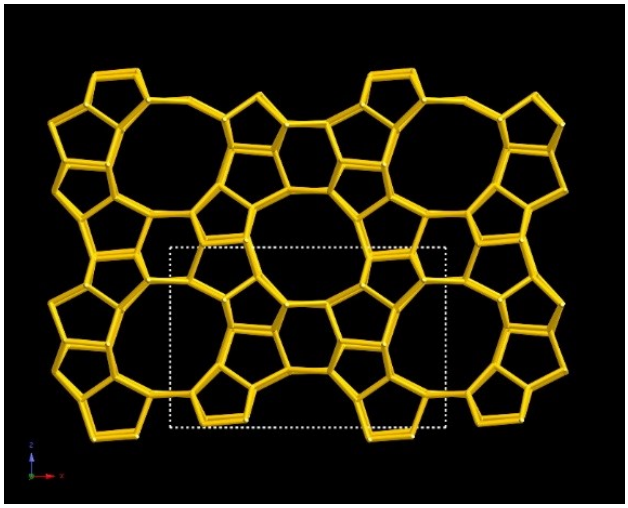

Figure 1: MFI zeolite framework viewed along [010].[9]

One of the main uses of TS-1 is in industrial scale oxidation reactions in the presence of hydrogen peroxide. This is due to its high reactivity and selectivity during oxidation reactions under mild conditions.[10] Addition of hydrogen peroxide to microcrystalline TS-1 leads to the formation of titanium peroxoderivatives.[11] Hydroperoxyl radicals generated by the Ti centres are then capable of decomposing reactants in solution via oxidation processes. Studies on the TS-1 catalysis have been carried out in the areas of epoxidation of olefins,[12] hydroxylation of aromatic compounds and phenol,[13] oxidations of alcohols and amines,[14,15] and oxidations of paraffins.[16] Reported data on catalytic characteristics of TS-1 vary significantly, this can be attributed to different characteristics of the samples used and differences in operating conditions. The ways in which variables in this complex system can influence reported findings can be summarized as: [17] (i) Ti content of the framework, as well as the presence of extra framework Ti can affect the relative rates of selective oxidation and H_2O_2 decomposition; (ii) Studies of reactions of molecules close in size to the size of the pore channels can lead to diffusion limitations which can obscure the intrinsic catalytic activity; (iii) Activity inside

or outside of the pore system; Shape selectivity effects favour conversions of small linear molecules over Ti^{IV} catalytic centres inside of the pores as observed in the low temperature epoxidation of olefins.[16] However, with larger molecules and higher temperatures it is possible that reactions can occur on Ti^{IV} located on the outer surface of the crystallites; (iv) Secondary reactions involving the initial reaction products reacting with H_2O_2 or other peroxocompounds formed in solution, or catalysed by centres other than Ti^{IV}; (v) High catalyst concentration favours selective oxidation, whereas high H_2O_2 concentration increases the rate of secondary reactions; (vi) Reaction temperature is critical; temperature dependences of intermediates will influence the reaction and composition of reaction products; (vii) Presence of impurities, for example Fe^{3+} and Co^{2+}, can catalyse H_2O_2 decomposition through the Fenton reaction and lower the selectivity. These impurities are effective catalysts at 5 to 10 ppm levels and therefore measures must be taken to ensure that reagents and laboratory apparatus are free from these impurities.

The effects of one or more of the above variables on catalytic activity can be seen in the work of Huybrechts *et al.*[18] For the degree of conversion of phenol in hydroxylation and the degree of conversion of 1-octene in epoxidation, it was observed that when Ti concentration is varied between 2.5 and 3 wt. % , correlations between catalytic properties and Ti content deviate from linearity. At higher Ti concentrations, there is an abrupt increase in the rate constant of H_2O_2 catalysed decomposition into water and O_2 which arises from the presence of unwanted anatase.

Application of TS-1 as a catalyst is due to isolated Ti^{IV} active sites, which have been isomorphically substituted into the zeolite framework in place of silicon. Evidence for this was found by comparing the unit cell volume (UCV) of TS-1 samples to pure silicalite-1 (S-

1). The relationship between UCV and the Ti content of the lattice is given by the equation:

$$V_x = V_{Si} - V_{Si}\left(1 - \frac{d_{Ti}^3}{d_{Si}^3}\right)x$$

where V_{Si} is the UCV of pure silicalite-1, d_{Ti} and d_{Si} (0.181 nm and 0.161 nm, respectively) are the tetrahedral Ti-O and Si-O bond distances and x is the atomic ratio Ti/(Si + Ti).[17] Substitution of Ti into the lattice structure is only valid up to 2.5 Ti per unit cell, as quoted in the original patent.[8] However, there is continuing discussion over the maximum possible limit of Ti incorporation into the zeolite framework.[19,20,21] By further increasing Ti content, it is often found that the Ti is not incorporated into the zeolite lattice, but appears as additional framework in the form of $Ti^{IV}O_2$. There is also difficulty preventing the precipitation of titanium dioxide during the crystallisation process.

1.2.1 SYNTHESIS OF TS-1

Two methods were described in the original patent for the hydrothermal synthesis of TS-1.8 The first method involves the synthesis solution being prepared by hydrolysis of tetraethyltitanate and tetraethylsilicate, whilst the second method uses colloidal silica and tetrapropylammonium peroxotitanate. For these methods, the presence of alkali cations, even in trace amounts, can prevent the substitution of Ti into the lattice.[22] Addition of NaOH to tetrapropylammonium hydroxide (TPAOH) leads to an increase in detected anatase and decrease of framework Ti species. Presence of the sodium species in the reaction mixture appears to favour the formation of insoluble titanium-silicate species, therefore reducing the amount of Ti available for the formation of TS-1. Factors such as the Si/Ti ratio and Si/TPAOH ratio of the precursor solution, the dilution of the

synthesis mixture and the temperature were found to influence the characteristics of the product TS-1. Synthesis of crystals with an average size of less than 100 nm is favoured by low crystallisation temperatures, a highly basic environment, diluted precursor solutions and low Ti content in solution, whilst higher temperatures form larger crystals but with lower Si/Ti ratio, and most of the Ti is present as extra-framework species (octahedral Ti^{IV} and anatase).

Introduction of mesoporosity into TS-1 samples has been studied in order to overcome the diffusion limitations imposed by the medium pore size of TS-1. Hierarchical TS-1 zeolites with enhanced catalytic activity from silanised protozeolitic unit have been prepared by Serrano *et al.*,[23] in which the mesopore size distribution could be reduced further by post synthesis treatment with cationic surfactants.[24] Porosity greatly affects the catalytic properties of titanosilicates; highly mesoporous materials are capable of promoting higher selectivity and allow products of catalysis reactions to more readily diffuse out of the pores, compared to materials with smaller pores.[25] However, one drawback to mesoporous titanosilicates is the leaching of Ti from active sites, which leads to the gradual deactivation of the catalyst. A disadvantage of preparing mesoporous TS-1 as a microcrystalline powder is recycling of the material after use in catalytic processes due to its powder form. A way to overcome this issue is preparation of hierarchically porous TS-1 materials in the form of macrostructures. This usually requires the use of colloidal synthesis solutions and sacrificial templates.

The use of colloidal zeolites in the preparation of zeolite structured materials is of great interest due to their easy processing.[26] Discrete TS-1 colloids formed from colloidal synthesis solutions are capable of diffusing into the interiors of mesoporous materials,

thereby using them as templates and allowing crystallisation to occur on the interior surfaces. Nanosized TS-1 crystals are normally synthesised using a clear precursor solutions in the presence of large amounts of organic structure-directing template (TPAOH). This provides discrete zeolite particles, often less than 100 nm in size and with narrow particle size distributions.[26] Colloidal suspensions of TS-1 have been prepared by Zhang *et al.*[27] A precursor clear solution was either (i) heated under reflux for 5-7 days at 100 °C or (ii) heated in an autoclave at a variety of temperatures in the range of 100-175 °C for 3-5 days.

As mentioned, tetrapropylammonium hydroxide is used as a zeolite structure directing template for the synthesis of TS-1. In addition to TPAOH, different sacrificial templates such as xerogels and carbon black have been used to create secondary porosity and sometimes macrostructures. The latter has been aimed at overcoming the difficulties of reclaiming or to suit a variety of catalytic roles. For instance, xerogels have been impregnated with solutions containing structure directing agent and heated in autoclaves at 170 °C for 2-72 h.[28,29] This method provides the benefit of allowing control of product homogeneity and Ti dispersion throughout the structure, along with reducing the chance of formation of anatase due to stabilization provided by the Si-O-Ti bonding structure of the xerogel. Investigation of synthesis factors such as impregnating solution/xerogel ratio, TPA^+/SiO_2 and OH^-/SiO_2 ratios, Si/Ti ratio and temperature has shown that all TS-1 formed through this method are capable of oxidative catalysis of n-hexane with H_2O_2. Another example of synthesis of hierarchical TS-1 is through the use of carbon black.[30] Similar to the xerogel method, carbon black is impregnated with TPAOH, tetraethoxytitanate (TEOT) and tetraethoxysilane (TEOS) solutions and then heated in an autoclave at 170 °C for 72 h. This method produces mesoporous (< 50 nm pore size) TS-1 crystals with a lattice fringe-

work running throughout the crystal structure. TS-1 produced via the carbon black method shows an increase in oxidative catalysis of cyclohexene, this is theorised to be due to better accessibility of the active sites. Hydrothermal preparation of TS-1 microspheres with the aid of a triblock copolymer template has recently been reported.[31] Microspheres formed were in the range of 50 to 100 nm and catalytic activity was comparable to conventional nanosized TS-1 for the epoxidation of 1-hexene and oxidation of pyridine in the presence of H_2O_2. TS-1 with a range of 140 to 200 nm were prepared through hydrophobicity control allowing for easy separation from the mother liquor.[32] A TS-1 synthesis gel was added to a silica and hexadecyltrimethoxysilane solution, which acts both as a silica source as well as a mesoporous template, and hydrothermally treated. Samples prepared showed excellent catalytic activity in the oxidation of bulky molecules such as benzothiophene and dibenzothiophene, compared to microcrystalline TS-1, due to the presence of mesopores allowing for greater mass transfer.

1.2.2 TS-1 PHOTOCATALYSIS

Although TS-1 has found use as an industrial catalyst in the presence of H_2O_2, photocatalytic applications of TS-1 are still very much in early stages of development. Previous studies have found TS-1 capable of photocatalytic decomposition of 4-nitrophenol and dibenzothiophene in the presence of hydrogen peroxide in an aqueous medium,[33,34] as well as photocatalytic degradation of monoethanolamine.[35] Efficiency of TS-1 as a photocatalyst is largely down to the presence of H_2O_2. In the absence of hydrogen peroxide, TS-1 samples comprised of lower Si/Ti ratios and large amounts of extra framework Ti produced high photocatalytic activity. With hydrogen peroxide

present, TS-1 samples with high Si/Ti ratios showed an enhanced rate of photocatalytic activity. This suggests that with H_2O_2 present, hydroxyl radicals are formed from interaction with framework Ti.[36] Comparisons of photocatalytic activity per unit weight of Ti was found to be lower for TS-1 than TiO_2, however activity per Ti atom was higher due to its zeolitic structure.[35]

The proposed mechanism for the photocatalytic reactions of TS-1 involves charge transfer excitation of the Ti active site, which is modified via adsorption of reactant species, prior to excitation by UV light. This can be shown as,

$$Ti^{4+} - O^{2-} \xrightarrow{h\nu} Ti^{3+} - O^{-}.$$ [35]

1.3 TITANIUM DIOXIDE

Titanium dioxide is a highly abundant material that has found use in many different applications from toothpaste to paints.[37,38] It is environmentally friendly, non-toxic, chemically stable and displays high reactivity. Since the discovery of its water splitting capabilities under UV light,[39] there has been a great emphasis on research into the potential photocatalytic and photovoltaic applications of TiO_2.

Titanium dioxide typically occurs in nature as the minerals rutile, anatase and brookite. The crystal structures of the TiO_2 minerals can be described in terms of the TiO_2 octahedrals which make up the crystal structure composition. Anatase is composed of octahedrals connected via vertices. In rutile, the edges of the octahedrals are connected, whilst in brookite, both the edges and vertices of the octahedrals are connected.[40] Anatase and rutile are the crystal phases most commonly used in photocatalytic applications. Anatase has the higher photocatalytic activity for most reactions.[41,42] This is

suggested to be due to anatase having a higher Fermi level, lower oxygen adsorption capacity and higher degree of hydroxylation.

Particle size plays a large role in the properties of a material. As improvements in nanoscience and nanotechnology are made, new physical and chemical material properties emerge as size decreases down to the nanometre scale. At the nano-scale, semiconductor properties emerge, also there is a dramatic increase in surface area per unit volume.[43] This surface area increase is beneficial to TiO_2 based materials, as it helps to improve rates of interaction between reactants and the TiO_2 materials. As the mounting pressure for humanity to become greener and more environmentally friendly, titanium oxide based materials are expected to play a major role in helping to solve environmental, pollution and energy issues.

1.3.1 SYNTHESIS OF TITANIUM DIOXIDE PHOTOCATALYSTS

TiO_2 photocatalysts typically come in the form of nanosized particles. For example, Degussa P25 and CristalACTiV™ PC500, are commercially available anatase based powders with particle sizes of 21 nm and 8 nm respectively. Degussa P25 and CristalACTiV™ PC500 are typically used as reference materials when testing the photocatalytic activities of new photocatalysts. Synthesis of nanomaterials normally involves the use of two fundamentally different methodologies, top-down; which involves the use of various techniques such as laser ablation, milling and sputtering to achieve the desired particle size, and bottom-up, which uses synthesis methods to produce the desired particle size.[44] This section will mainly focus on the bottom-up methods of production.

Hydrothermal and solvothermal synthesis methods, which involve the use of aqueous and non-aqueous solvents respectively, are performed using autoclaves where

temperatures can be raised above the boiling point of the solvent. In this respect solvothermal methods have an advantage over hydrothermal, since the use of organic solvents with boiling points much higher than water can be used.[45] Via these two methods, a wide range of materials can be produced, with specific material properties based on the solvent mixture and Ti content used during synthesis. For example, Zhang *et al.* synthesised TiO_2 nanorods through hydrothermal treatment of low concentration titanium tetrachloride in the presence of inorganic salts or acid.[46]

Dielectric materials, such as those containing TiO_2, can be produced using high frequency microwaves. Frequencies used are between 900 and 2450 MHz. Microwave synthesis provides advantages due to rapid heat transfer, volumetric and selective heating, and is relatively cost effective. Colloidal titania nanoparticle suspensions were prepared after 5 min to 1 h of microwave irradiation, whilst conventional hydrolysis at 195 $^{\circ}$C requires up to 32 h.[47] TiO_2 nanotubes have also been prepared via microwave synthesis by Wu *et al.*[48] Nanotubes were prepared via reduction of TiO_2 crystals of anatase, rutile or mixed phases. Nanotubes produced had hollow centres, were open ended and multiwalled structures with 8-12 nm diameter and 200-1000 nm lengths.

Mesoporous/nanoporous TiO_2 materials have been studied in the last decade, with and without the use of surfactant templates. Mesoporous amorphous TiO_2 beads have been prepared by Chen *et al.* using hexadecylamine (HDA) as a structure directing agent via a combined sol-gel and solvothermal method.[49] The amorphous TiO_2 beads were photocatalytically evaluated by degradation of methylene blue under UV light and were found to have a similar activity to Degussa P25.[50] Preparation of three dimensional thermally stable mesoporous TiO_2 without the use of surfactants has been achieved by Yu *et al.*[51] TiO_2 nanoparticles were formed by ultrasound assisted hydrolysis of acetic acid

modified titanium isopropoxide. These nanoparticles were then directed to form spherical or globular particles via controlled condensation and agglomeration, under high-intensity ultrasound radiation. However, the materials produced lacked long range order. Zhuang *et al.* showed that Ti-containing hexagonal mesoporous silica (Ti-HMS) displays better photocatalytic activity than commercially available Degussa P25, when decomposing benzene in the gas phase.[52] There was also no observed deactivation of the photocatalyst over a 12 h testing period.

Templating methods have been studied by various groups.[53] [54] [55] These methods employ organic agents in order to aid the organization of network forming metal oxides in non-aqueous solutions. For instance, amphiphilic alkylene oxide copolymers are commonly used as organic templates. Organic templates were dissolved in ethanol and $TiCl_4$ added under vigorous stirring. The resulting sol solution was gelled in air at 40 °C for 1 -7 days. Samples were calcined to remove organic components and the mesoporous TiO_2 was obtained.

1.3.2 TITANIUM DIOXIDE PHOTOCATALYSIS

The use of TiO_2 for photocatalytic degradation of pollutants is well documented.[56,57,58] Figure 2 shows the proposed photocatalytic mechanism for TiO_2 photocatalysts. Activation of the catalyst involves promotion of an electron (e^-) from the valence to conduction band via photoexcitation; the resulting e^- and hole are then available to be used in redox processes by reactants adsorbed to the material surface. However, the redox processes are in competition with the e^-/hole recombination, which can have an effect on photocatalytic efficiency of materials. Figure 2 can be summarised

as follows. Upon irradiation with UV light e^- and holes (h^+) are produced in the conduction (CB) and valence bands (VB):

$$TiO_2 + h\upsilon \rightarrow TiO_2\ (e^-_{CB} + h^+_{VB})$$

The positively charged h^+ can oxidize hydroxide ions to produce hydroxyl radicals on the surface of the catalyst:

$$TiO_2\ (h^+_{VB}) + H_2O \rightarrow TiO_2 + H^+ + \bullet OH$$

The e^- can react with oxygen to produce superoxide radical anions, which can then protonate to form hydroperoxyl radicals:

$$TiO_2\ (e^-_{CB}) + O_2 \rightarrow TiO_2 + O_2^{-\bullet}$$

$$O_2^{-\bullet} + H^+ \rightarrow HO_2\bullet$$

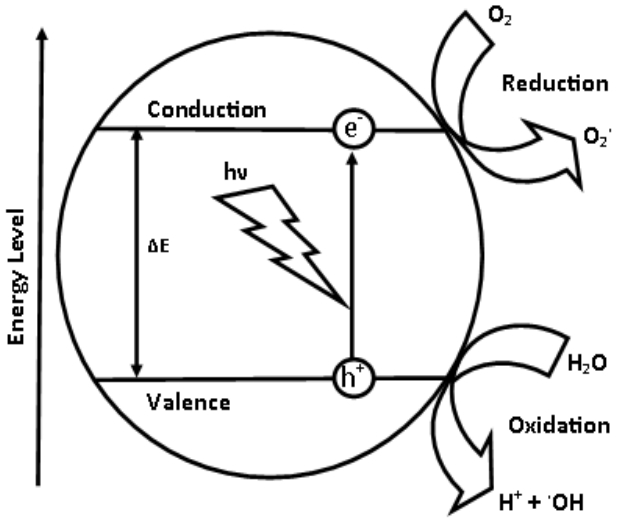

Figure 2: Titanium dioxide photocatalytic mechanism[59]

Doping TiO_2 with metal ions presents one potential solution to the problem of e^-/hole recombination by introducing electron capture centres. This results in a reduction

of e^-/hole recombination centres, by introducing defects to the crystal structure, thereby increasing photocatalytic efficiency.[59] Recently, Yan *et al.* synthesised TiO_2 nanoparticles doped with cerium ions.[60] It is suggested that additional electronic states are generated by the Ce ion in the band-gap of TiO_2, which capture the photoformed holes and therefore decreasing the rate of e^-/hole recombination. Metal ion doping also has the potential to help shift TiO_2 photoactivity into the visible light spectrum via photosensitization. Iron doped anatase TiO_2, prepared and tested by Zhang *et al.*[61] has been used for the photocatalytic degradation of active yellow XRG dye. Results indicate the amount of doped iron plays a significant role in affecting the photocatalytic activity of TiO_2 and, at optimum levels, is capable of enhancing visible light photocatalytic activity.

Particle size plays an important role photocatalytic efficiency of a material, with a decrease in size the number of atoms located at the surface of a material increases due to high surface area to volume ratios. Wang *et al.* demonstrated that that there was an optimal size for TiO_2 nanoparticles for maximum efficiency in photocatalytic decomposition of chloroform.[62] Activity increased when size was decreased from 21 nm to 11 nm, but activity decreases once particle size is reduced further to 6 nm. In larger TiO_2 nanoparticles, bulk recombination of charge carriers is the dominant process. As particle size decreases, surface recombination becomes the dominant process since generation of the electrons and holes occurs at the surface, this process of surface recombination is faster than interfacial charge carriers processes.[63]

1.4 RESIN TEMPLATING

Upon reduction of particle size there is the overbearing issue of difficulty in reclaiming the catalyst after a reaction. Nanosized particles suspended in liquids are

extremely difficult to remove with the use of filters and sieves, and normally require centrifugation at high speeds. Resin templating provides a solution to this issue; use of an ion exchange resin as a sacrificial macrotemplate can produce self-bonded macrostructures which are similar in size and shape to the resin template used. These macrostructures can easily be removed from reaction solutions via sedimentation. General method for production involves mixing of resin beads with synthesis solutions, followed by calcination to remove organic components and create secondary porosity within the sample.

Use of ion exchange resins as macrotemplates has previously been studied for the synthesis of silicalite-1, ZSM-5 and zeolite beta.[64,65,66,67] It was found that crystalline macrostructures can be formed from macroporous resins, whilst amorphous macrostructures are formed when gel resins are used. Shrinkage of macrostructures occurs upon calcination when a weakly basic anion exchange resin is used instead of a highly basic resin, thus use of a highly basic ion exchange resin is preferred. Reduction of resin to solution weight ratio also leads to a decrease in sample crystallinity.

Zeolite crystallisation within macroporous resins is a complex process as the resin is not inert in the process. Crystallisation in samples is affected by the synthesis solution, resin to solution weight ratio, temperature and treatment time. Highly crystalline samples are usually prepared using temperatures >100 °C. A two-step synthesis method has been used to produce fully crystalline silicalite-1 beads of high mechanical strength, in which treatment at a lower temperature is followed by a second treatment at a higher temperature.[66]

Resin templating has also been applied to the synthesis of titanosilicates. Bimodal mesoporous titanosilicate beads (BMB-TiSil) were synthesised in the presence of an anion

exchange resin.[68] BMB-TiSil samples showed a higher turnover frequency of alkene conversion for epoxidation reactions in the presence of aqueous H_2O_2 than Ti-MCM-41. There was also no notable loss of activity after three consecutive tests. Amorphous titanosilicate beads with incipient TS-1 features (TiSil-HPB-60) have been produced through resin templating.[69] X-ray patterns of TiSil-HPB-60 beads showed amorphous material present, which is indicative of a lack of a crystalline zeolite lattice structure. However, when evaluating catalytic activity, TiSil-HPB-60 produced higher epoxide yields than TS-1 and Ti-MCM-41 samples in the presence of aqueous H_2O_2. Macroscopic amorphous TiO_2-SiO_2 beads, containing different amounts of TiO_2 as an active phase, have been synthesised by Cani and Pescarmona.[70] Samples with a Ti : Si ratio of less than 40% showed no crystalline anatase. However, samples with a Ti : Si ratio of 40% to 70% contained TiO_2 crystallites in the range of 12 to 64 nm. When evaluated for photocatalytic activity using first order degradation kinetics of methylene blue and phenol under UV light, the macrostructures performed more effectively than P 25. It was found that photocatalytic activity is related to the Ti content of the samples and the catalyst surface area.

1.5 BET MODEL AND ADSORPTION ISOTHERMS

The Brunauer, Emmett and Teller (BET) isotherm is commonly used to calculate the surface areas of solid materials analysed by gas adsorption. The BET theory can best be described by the following equation,

$$\frac{p}{V(p_0 - p)} = \frac{1}{V_\infty C} + \frac{C-1}{V_\infty C}\left(\frac{p}{p_0}\right)$$

where is the volume of adsorbed gas, V_∞ is volume of gas adsorbed corresponding to a monolayer, p/p_0 is the relative pressure, and C is the BET constant which is given by the equation,

$$C = exp\frac{E_1 - E_L}{RT}$$

where E_1 is the heat of adsorption for the first layer, E_L is equal to the heat of liquefaction, R is the molar gas constant and T is the temperature at which the process is occurring. The linear relationship of the BET equation is maintained when $0.05 < \frac{P}{P_0} < 0.35$.

Adsorption isotherms have been classified into five types according to the Brunauer, Deming, Deming and Teller (BDDT) system (Figure 3).[71]

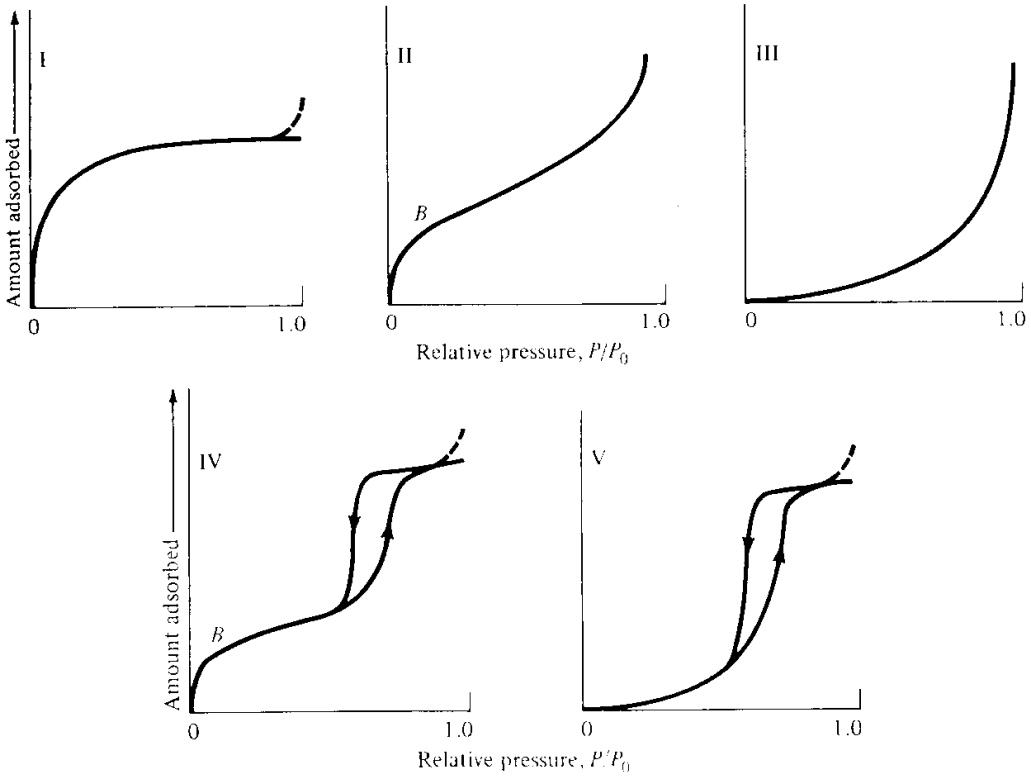

Figure 3: The five types of adsorption isotherms according to the BDDT classification.[71]

Microporous materials such as zeolites show type I isotherms, which is characterised by a steep increase in the volume adsorbed at low relative pressures followed by a plateau. Micropores do not allow multilayer adsorption because of their size resulting in a Langmuir-type isotherm. Mesoporous materials have type IV isotherms with a hysteresis loop associated with capillary condensation of the gas in mesopores resulting in different volumes of gas adsorbed measured during adsorption and desorption. The materials prepared in this work show a mixture of type I and IV isotherms due to the presence of micropores and mesopores (Section 3.1.2).

1.6 ORGANIC POLLUTANTS IN WATER

Removal of dyes and other organic pollutants from waste water is becoming a growing issue. Due to their high solubility in water, up to 20% of the total world production of dyes is lost during the dying process and can be found in trace quantities in industrial wastewater.[72,73] Current technologies involve the application of traditional physical techniques (Adsorption on activated carbon, reverse osmosis, ultrafiltration, etc.),[74] and as such provide no real solution to the issue. This is due to capture and storage of dyes and pollutants being non-destructive, and creating secondary pollution by moving organic pollutants from water to another phase.

Photocatalytic degradation of pollutants using TiO_2 based catalysts has proven to be an environmentally friendly and sustainable method of dealing with harmful chemicals found in the water supply.[75,76,77]Advantages of using Ti based catalysts is their ability to operate under ambient temperatures and pressures, along with complete mineralisation of pollutants. However, these materials tend to be nanosized particles and as such; suffer from aggregation and separation issues which reduces the catalyst efficiency.

Methylene blue (MB) (Figure 4) is a toxic dye commonly used in the textile industry with an extremely prominent colour, even at very low concentrations. MB is also commonly used to evaluate the photocatalytic activity of new photocatalytic materials.[78,79,80]

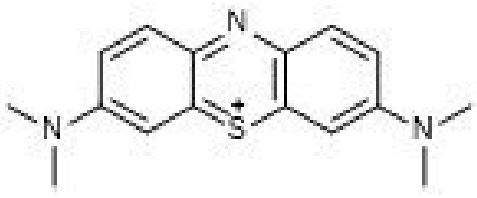

Figure 4: Methylene Blue molecule.

UV-Vis spectrophotometry is used to measure the first order degradation kinetics of MB in the presence of photocatalysts under UV irradiation; this is due to MB having a very strong absorbance peak at 665 nm which can be easily tracked. The absorbance peak at 665 nm arises due to the hetero-polyaromatic linkage present in MB. The peak at 665 nm also exhibits a shoulder at 615 nm, which corresponds to monomers and dimers respectively.[81] The mechanism of MB degradation in the presence of Ti based catalysts has been studied in detail can be summarised as follows.[82] Photoexcitation of MB injects an e^- into the conduction band of the TiO_2:

$$MB^* + TiO_2 \rightarrow MB^{+\bullet}\ e^-_{CB}(TiO_2)$$

$$O_2 + e^- \rightarrow\ O_2^{-\bullet}$$

The MB dye is then converted to a cationic radical that undergoes degradation:

$$MB^{+\bullet} + {}^-OH \rightarrow MB + \bullet OH$$

$$MB^{+\bullet} + \bullet OH \rightarrow \text{degradation products}$$

$$MB^{+\bullet} + O_2^{-\bullet} \rightarrow \text{degradation products}$$

1.7 AIM

The aim of this study was to prepare hierarchically porous TS-1 macrostructures and to evaluate their photocatalytic activity. The work was broken up into the following stages:

- The initial stage was to optimise synthesis of hierarchically porous TS-1 macrostructures, using an anionic exchange resin as a sacrificial template, in terms of crystallinity and mechanical stability.
- Secondly, characteristics of TS-1 macrostructures were determined by methods such as X-ray diffraction (XRD), Scanning electron microscopy (SEM), nitrogen adsorption, Raman analysis and Energy dispersive X-ray spectroscopy (EDX).
- Photocatalytic activity of the TS-1 beads was measured using first order kinetics of methylene blue degradation under UV light . Photocatalytic activity of the TS-1 macrostructures was also compared to that of a commercial TiO_2 anatase nanopowder. The reusability of the TS-1 catalysts in the photocatalytic reaction was also evaluated.
- Finally, data collected was analysed in order to relate the photocatalytic activity to the characteristics of the TS-1 beads.

2 EXPERIMENTAL

2.1 TS-1 SYNTHESIS

TS-1 macrostructure synthesis was achieved through the use of a clear synthesis solution with molar composition of, 9TPAOH : $xTiO_2$: $25SiO_2$: $404H_2O$, where x= 0.25, 0.5 or 1.0.[27] Preparation of the synthesis solution was done by mixing tetraethoxysilane (TEOS) (Sigma, 98%) with tetraethoxytitanate (TEOT) (Lancaster Synthesis, 98%). Structure directing agent tetrapropylammonium hydroxide (TPAOH) (Alfa Aesar, 1M aqueous solution) was then added dropwise to the synthesis solution in order to prevent the formation of anatase, at a rate of 1 ml/min. Once the TPAOH had been added, the TS-1 synthesis solution was left to hydrolyse for one hour, using vigorous stirring.

After hydrolysing, Amberlite IRA-900, a strongly basic macroporous anionic exchange resin (Alfa Aesar) was added to the synthesis solution, in a solution to resin weight ratio of 10. The mixture was then sealed into a PTFE-lined stainless steel autoclave and hydrothermally treated using a two stage temperature synthesis, initial stage is treatment for 48 h at 100 °C and then increasing the temperature to 170 °C for 6 h for the second stage.[83]

After synthesis, the TS-1/ion exchange resin beads were separated from the mother liquor by decanting, rinsed with distilled water and ultrasonicated to remove any loose bulk phase material, dried and then finally calcined at 600 °C for 10 h to remove organic components, after heating to this temperature at a rate of 10°C/min. The samples obtained were denoted as TS-1(0.25), TS-1(0.5) and TS-1(1.0) corresponding to the different x used in the molar composition of the synthesis solution.

A silicalite-1 reference sample with molar composition 9TPAOH : 25SiO_2 : 480H_2O was prepared using the same method as TS-1, with a hydrothermal treatment at 100 °C for 17 h followed by treatment at 170 °C for 10 h.

2.2 CHARACTERISATION

Scanning Electron Microscopy (SEM) was used to study the morphology of the macrostructures. SEM was carried out using a Supra 40VP microscope from Carl Zeiss Ltd. In order to measure the Ti content of the prepared beads energy-dispersive X-ray (EDX) spectroscopy was carried out using an Apollo 40 SDD detector from EDAX Inc. The average of five measurements was taken from uncoated discs formed from ground up beads. X-ray Diffraction (XRD) patterns were obtained from ground samples using an X'Pert PANalytical X-ray Diffractometer with a Cu Kα X-ray source (40 kV and 30 mA) and a PIXcell detector. Nitrogen absorption measurements were performed at -196 °C using a Micromeritics ASAP 2020 surface area analyser on the calcined TS-1 spheres and bulk TS-1 samples. Samples were outgassed at 300 °C for 12 hours prior to analysis. Surface areas and pore size distributions were then calculated using the BET equation and BJH (desorption branch of the isotherm) method, respectively. Total pore volumes (V_{total}) were obtained from the volume adsorbed at a relative pressure of 0.99, whereas micropore volumes (V_{μ}) and external surface areas (S_{EXT}) were determined from t-plot analysis. To study the Ti phases present in the samples, Raman spectroscopy was performed on TS-1 and S-1 beads, and CristalACTiV™ PC500. Raman measurements were carried out with a Horiba Jobin-Yvon T64000 triple-monochromator spectrometer equipped with a LN_2-cooled Symphony CCD detector and an Olympus BH41 microscope with a 50x long-working distance objective. Spectra were collected in the range of 15 –

4000 cm^{-1} using a 514.5 nm Ar^{+}-ion laser (Coherent Innova 90C FreD). Laser power on the surface of the samples was 5.9 mW, whilst the laser spot diameter was 2 μm approximately. Achieved spectral resolution was 1.9 cm^{-1}, while the precision of peak positions was 0.35 cm^{-1}. Excitation with a beam of wavelength 488.0 nm proved that all observed peaks arise from atomic vibrations instead of photoluminescence. Measured spectra were baseline corrected for the continuum photoluminescence background and temperature-reduced to account for Bose-Einstein occupation factor. Microwave resonance broadband dielectric loss (BDS) measurements with simultaneous UV irradiation were undertaken using a Marconi (6200A) 2-20 GHz programmable sweep generator and automatic amplitude analyser, coupled to a rectangular waveguide and cylindrical cavity. CristalACTiV™ PC500 and TS-1(0.25) samples (0.2 g) placed in the cavity were irradiated in the cell chamber with an ILC 302UV xenon source (Laser Lines Ltd.) via an optical fibre and data corrected for sample density. Attenuation of the power stored by the microwave cavity (± 0.05 dBm) was monitored at 25 °C in real-time during 1800 s of irradiation and then for a further 1800 s with the light-source switched-off.

2.3 PHOTOCATALYTIC TESTS

Evaluation of the photocatalytic activity of the TS-1 macrostructures was performed using first order degradation kinetics of methylene blue (MB) (BDH chemicals) under UV light. Stock MB solutions with concentrations of 0.03 to 0.4 mM were prepared and used within one week of preparation. 10 ml of MB was added to 0.2 g of TS-1 macrostructures, the samples were then placed on a gyratory shaker (Stuart Scientific, 100 RPM, 35 °C) for three hours, in the dark, in order to equilibrate dye concentration in solution by accounting for adsorption of the dye into the pore structure of the TS-1

macrostructures. For comparison, the photocatalytic activities of CristalACTiV™ PC500 (100% anatase, BET surface area of 345 $m^2 g^{-1}$, particle size of 5-10 nm) and Silicalite-1 (S-1) were also evaluated. Due to the lower adsorption capacity of PC 500, 3.0×10^{-5} M MB was used for measuring degradation kinetics of MB.

After equilibrating, the samples were then placed into an Atlas Suntest CPS+ cabinet (1500 W Xe UV lamp) and irradiated in 15 minute doses, at 400 W/m^2 and 35 °C. After irradiation, the samples were removed from the cabinet and aliquots of dye were removed for UV-Vis analysis. Due to the small particle size of CristalACTiV™ PC500, centrifugation (MSE Mistral 2000, 3632 G, 5 min) was used to separate it from the mother liquor. Six samples of CristalACTiV™ PC500 were prepared and used for individual UV-Vis measurements to avoid mass loss errors caused by centrifugation. UV-Vis measurements were performed using an Agilent Cary 8454 UV-Vis spectrophotometer (W and D lamps), measuring absorbance at 665 nm. After UV-Vis measurements, the aliquots of dye were returned to the irradiation vials and samples were irradiated with the next 15 minute dose. This continued until absorbance measurements at 665 nm were <0.1 Arb. Units. Vials were equilibrated at 35 °C prior to returning to the Suntest cabinet. The same experimental conditions were applied to MB solution without the presence of a catalyst. During preliminary experiments, the initial MB concentrations were adjusted so that post-adsorption dye concentration was around 0.03 mM for all samples.

To determine reusability of the TS-1 samples, decoloured MB solutions were decanted and replaced with fresh MB solutions, without washing or any other laboratory procedures. This was carried out a total of four times. TS-1 beads retained their bright blue colour after initial MB adsorption. Experiments were also performed after regenerating the beads at 600 °C for 10 h.

3 RESULTS AND DISCUSSION

3.1 SYNTHESIS OF TS-1 BY RESIN TEMPLATING

3.1.1 EFFECTS OF TIME AND TEMPERATURE

The effect of hydrothermal treatment time and temperature on the crystallinity and mechanical stability of the samples was firstly studied. Figure 5 shows the XRD patterns of TS-1 macrostructures obtained through direct synthesis at a single temperature of 100 °C or 170 °C. TS-1 - 170/48 prepared at 170 °C for 48 h showed high crystallinity, whereas TS-1 - 100/168 prepared at 100 °C for 68 h showed a large amount of amorphous material present in the sample, as indicated by the large amorphous halo.

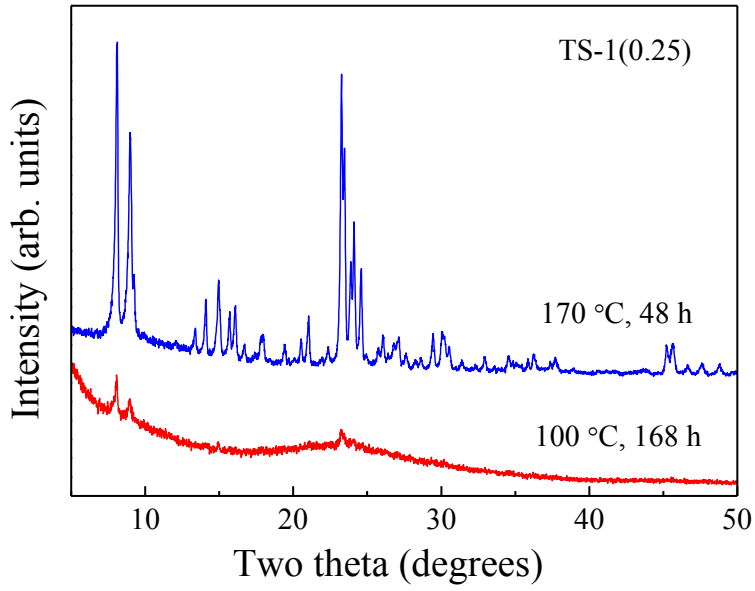

Figure 5: XRD patterns of TS-1(0.25) produced via direct synthesis with treatment at 100 °C or 170 °C.

The TS-1 macrostructures prepared at 170 °C were extremely fragile. Figure 6 shows an SEM micrograph of these structures. As seen, the particles were hollow, which

was the reason for their brittleness. Hollow macrostructures arise from diffusion limitation issues of zeolite nutrients and exterior crystal growth at the expense of zeolite nutrients from the interior of the beads as previously observed in the synthesis of ZSM-5 by resin templating.[66] Nutrients diffuse into the template interior via ion exchange. Exterior crystal growth then occurs on the template surface by consuming the nutrients which have been initially ion exchanged into the template interior. The rate of diffusion of nutrients into the template interior is therefore in direct competition with the rate of crystallisation.

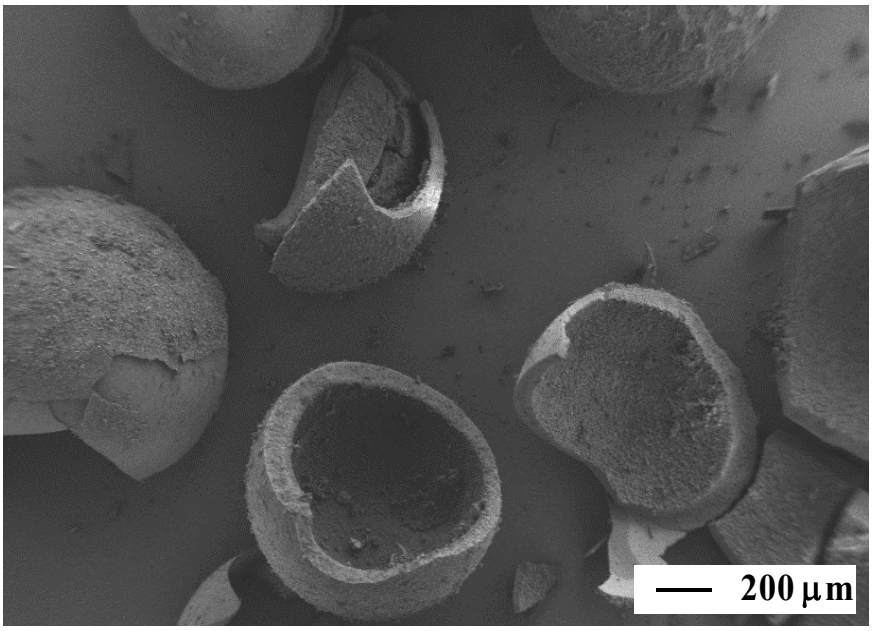

Figure 6: SEM micrograph of hollow TS-1 macrostructures obtained via direct synthesis at 170 °C.

A two-step synthesis procedure 100 °C – 170 °C was employed to increase TS-1 crystallinity compared to samples prepared directly at 100 °C, without affecting their mechanical stability.[66] The initial treatment at 100 °C was fixed at 48 h and the secondary treatment at 170 °C was varied between 6 and 12 h. Mechanical stability of product beads was inspected visually during grinding. Crystallinity of samples decreased with a

decrease in the treatment time at 170 °C (Figure 5) as can be seen by the decrease in peak intensity. The beads produced after 7 h of treatment were still fragile, whereas the beads prepared after 6 h were stable. The 6 h treatment time was therefore chosen for the preparation of subsequent samples.

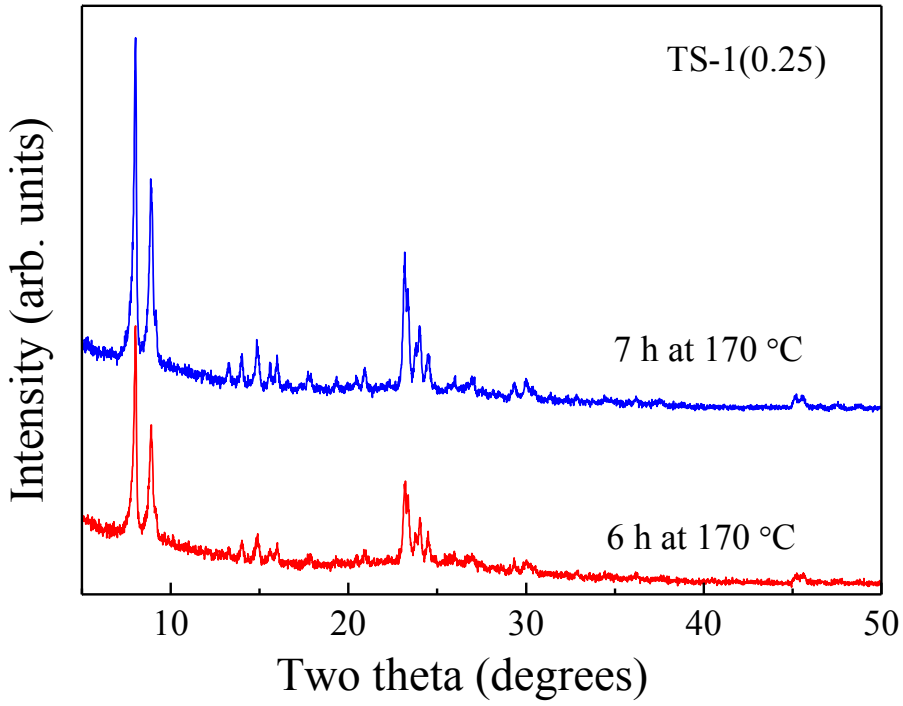

Figure 7: Effect of the second stage synthesis duration on TS-1 crystallinity.

3.1.2 EFFECT OF TI CONTENT

Figure 8 shows XRD patterns of TS-1 samples prepared using the two stage synthesis, with a secondary heating stage of 6 h at 170 °C. XRD results show that all Ti-containing samples contain crystalline phases of MFI-type zeolite and a large amount of amorphous material. Assuming S-1 to be 100% crystalline, comparisons of the peak areas of the MFI diffraction peaks in the range 22-25° 2θ showed decreasing crystallinity from 19% to 9% as Ti content increases from TS-1(0.25) to TS-1(1.0) respectively.

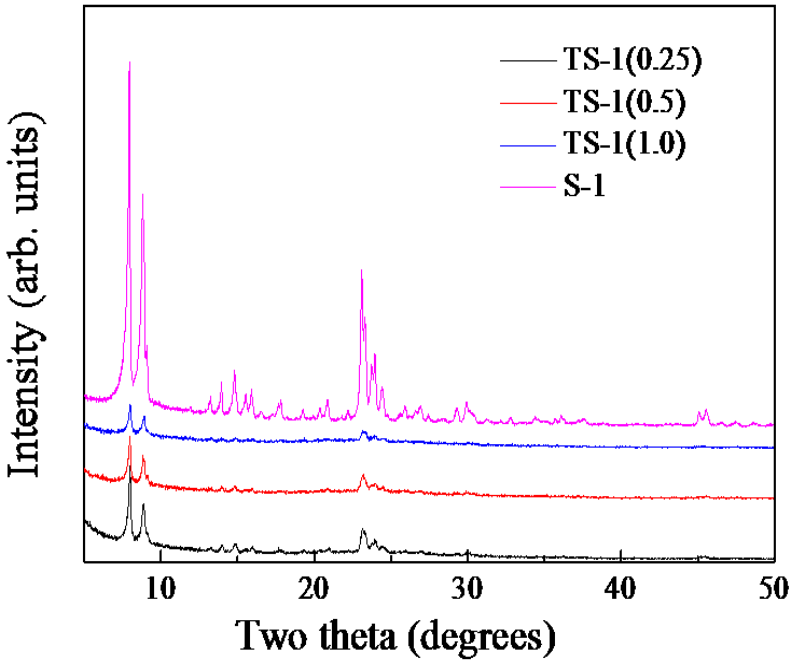

Figure 8: XRD patterns of S-1 and TS-1 samples.

In order to characterise the different phases of Ti present in the macrostructures, Raman spectroscopy was employed. Figure 9 shows representative Raman spectra of TS-1 samples, as well as S-1 and CristalACTiV™PC500 reference samples. In the case of TS-1(1.0), two types of spectra were measured indicating inhomogeneities .The reference S-1 sample showed a typical Raman spectrum of a highly crystalline S-1 with an intense peak at 380 cm^{-1}.[64] This peak is seen in the TS-1 samples as well together with a Raman scattering near 495 cm^{-1} associated with the presence of an amorphous material. The intensity of the latter is increasing with increasing Ti content is in agreement with the XRD results. The Raman peak at 3750 cm^{-1}, due to surface silanol groups, decreases with increasing Ti content and is absent in TS-1(1.0). Relative intensity of this peak depends on the surface-to-bulk ratio and is indicative of the presence of small grains, which is in agreement with the external surface areas measured for TS-1(0.25) and TS-1(0.5) (see

further, Table 1). Peaks at 150 cm^{-1}, 400 cm^{-1}, 515 cm^{-1} and 640 cm^{-1} are indicative of pure anatase, as can be seen in the case of CristalACTiV™PC500. [84,85] The anatase peak at 150 cm^{-1} can also be seen clearly in one of the spectra for TS-1(1.0), indicating presence of an anatase impurity phase.

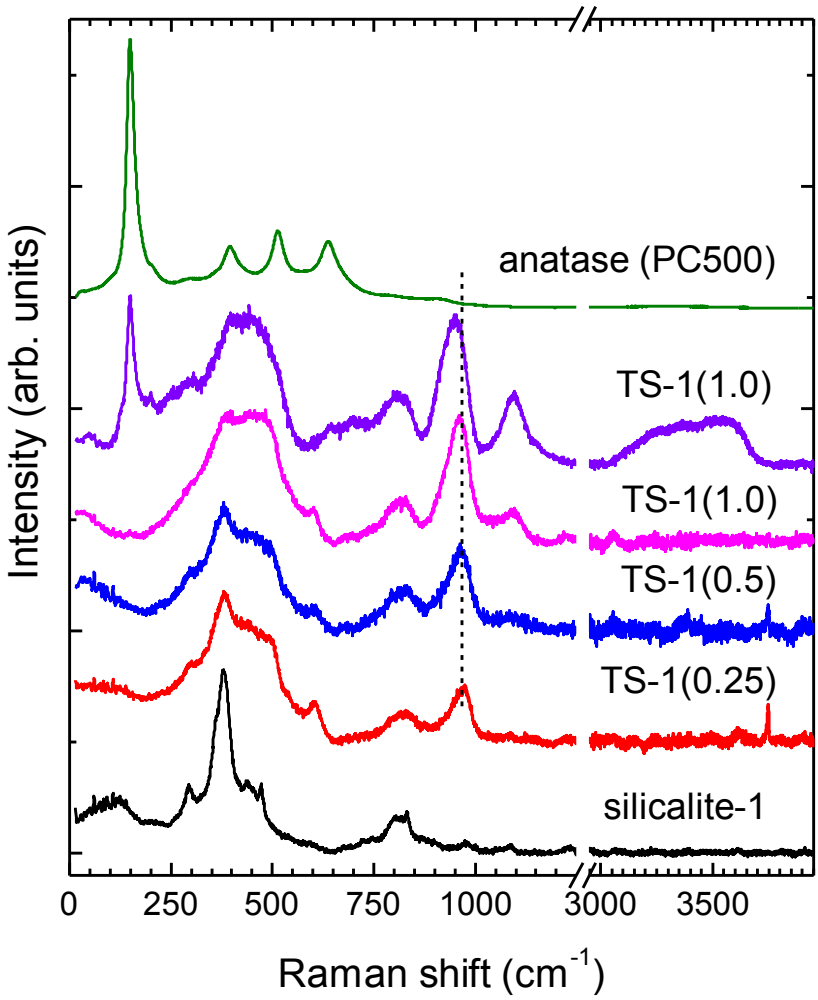

Figure 9: Raman spectra of TS-1 beads, and S-1 and CristalACTiV™ PC500 reference samples. Spectra are vertically offset for clarity and a dashed line at 960 cm^{-1} has been added to indicate Ti substitution into the lattice framework.

The intensity of the peak at 960 cm^{-1} observed in the Raman spectra of all TS-1 samples, is well correlated with Ti which has been incorporated into the lattice structure.[19,86] The peak intensity increases with increasing Ti content. A shift of the 960

cm^{-1} peak to lower wavenumbers was observed for one of the TS-1(1.0) Raman spectra, which could be explained by the presence of water.[87] The broad band between 3200 and 3600 cm^{-1} confirms the presence of water in TS-1(1.0).

The effect of titanium content on the morphology of the TS-1 beads was studied through the use of SEM. All TS-1 beads produced were similar in size and shape to the ion exchange resin beads used as a template (Figure 10). A small number of cracked and broken beads was present in TS-1(0.25) and TS-1(0.5) samples, this number was higher for TS-1(1.0).

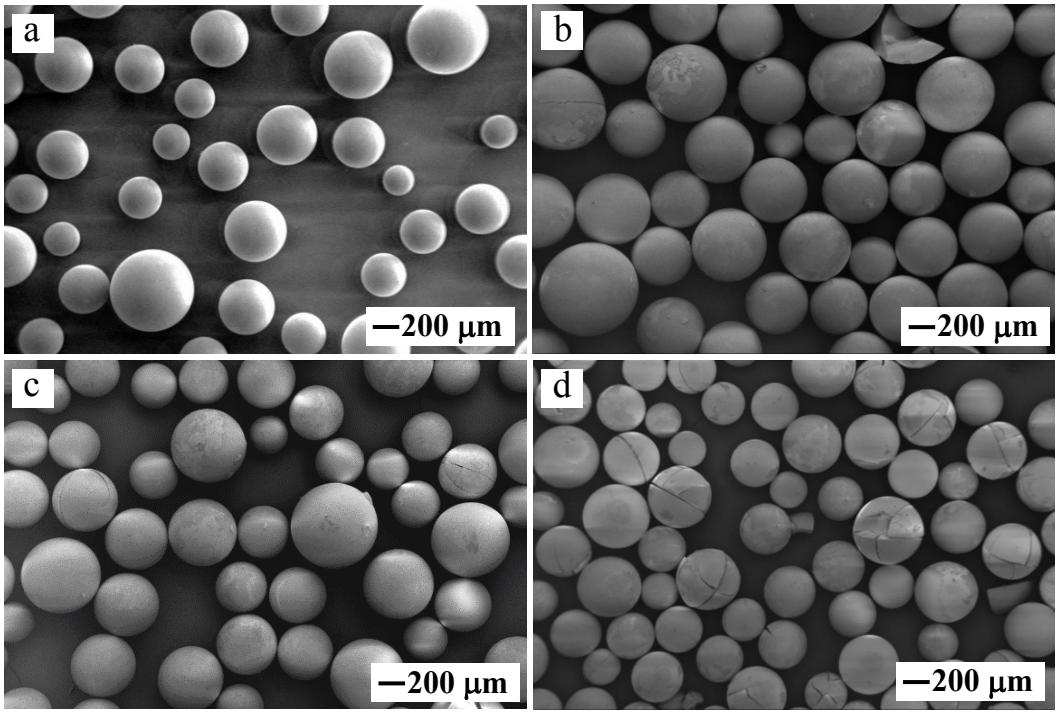

Figure 10: SEM micrographs of: (a) the resin template, (b) TS-1(0.25), (c) TS-1(0.5) and (d) TS-1(1.0).

The interior of the beads were built from fine nanoparticles (Figure 11). The interior structure did not change between samples and was independent of the sample Ti content. This has been observed for all zeolitic materials prepared via the resin

templating method.[64,65,66] Crystal growth in the resin interior is restricted by the resin polymer chains and is limited to the size of the resin macropores, which is around 100 nm. However, crystal growth on the surface of the beads is not restricted and larger crystals displaying the typical orthorhombic shape of the MFI-type morphology can be seen (Figure 12). As Ti content of the samples increases, there is a noted decrease in crystal size. For TS-1(1.0), two distinct surface morphologies can be observed. This is an indication that the sample is not as homogenous as TS-1(0.25) and TS-1(0.5) as observed by Raman analysis.

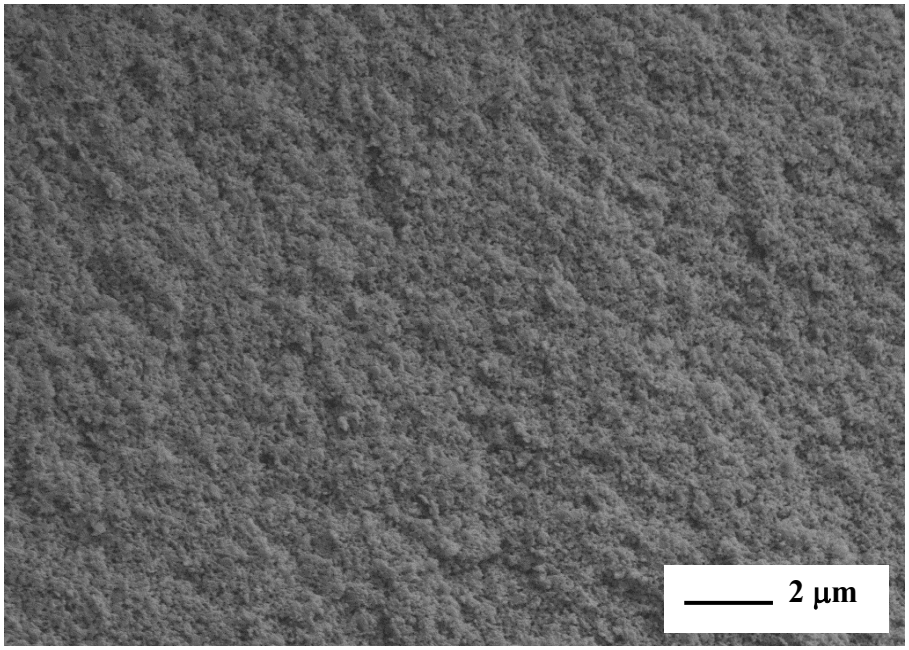

Figure 11: Representative SEM image of TS-1 beads interior.

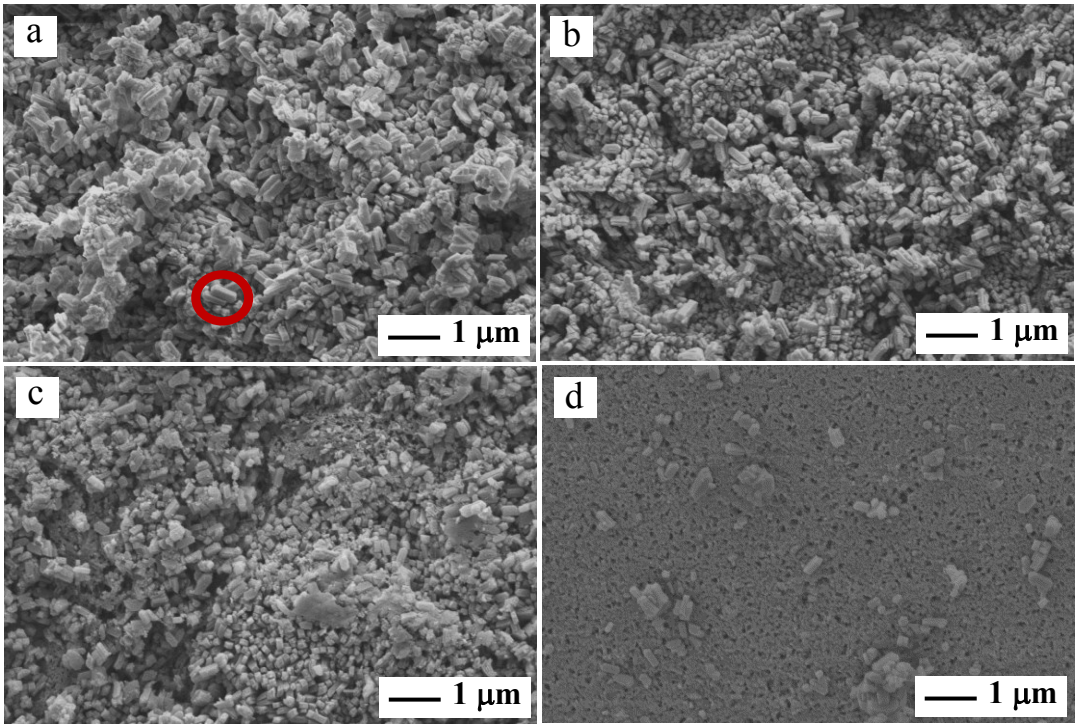

Figure 12: SEM micrographs of the surface of: (a) TS-1(0.25), (b) TS-1(0.5) and (c,d) TS-1(1.0). An example of orthorhombic shape crystals typical of MFI-type materials has been circled in red.

Figure 13 shows nitrogen adsorption isotherms of TS-1 samples. The beads display type I/IV isotherms. Hysteresis loops present at high relative pressures are an indicator of the presence of mesopores in the beads. The steep gradient of gas adsorption at low relative pressures, as well as the horizontal plateaux, seen in the isotherms is evidence of the microporous structure of the TS-1 beads. Pore size distribution measurements (Figure 14) of the beads showed the presence of mesopores in the range of 20 to 50 nm. There is no indication that there are any substantial differences in the secondary porosity of the samples, which is in agreement with the SEM observations of the interior structure of the beads. This is due to the secondary porosity of the samples being introduced by removal of the resin.

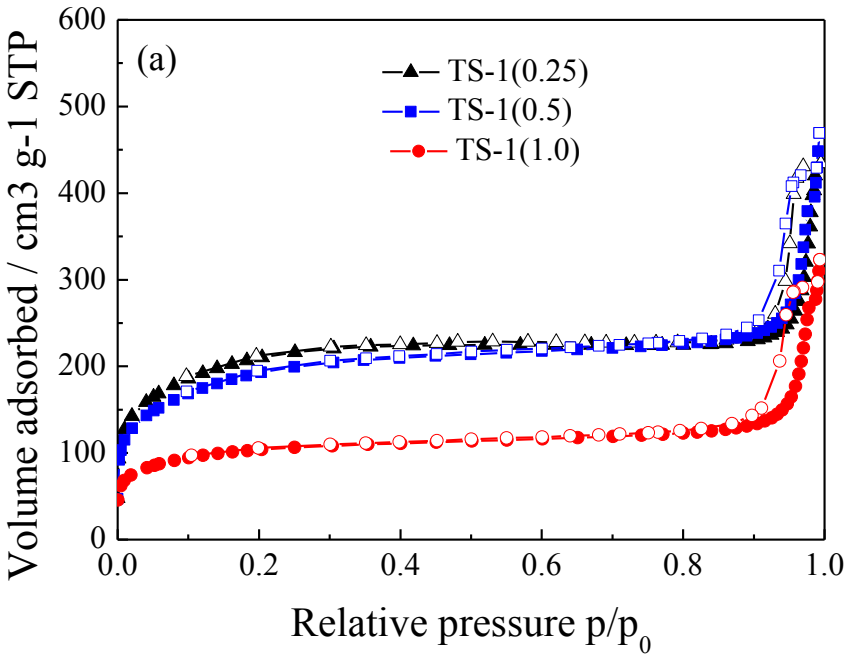

Figure 13: Nitrogen adsorption isotherms at -196 °C for TS-1 beads (Closed symbols = adsorption and open symbols = desorption).

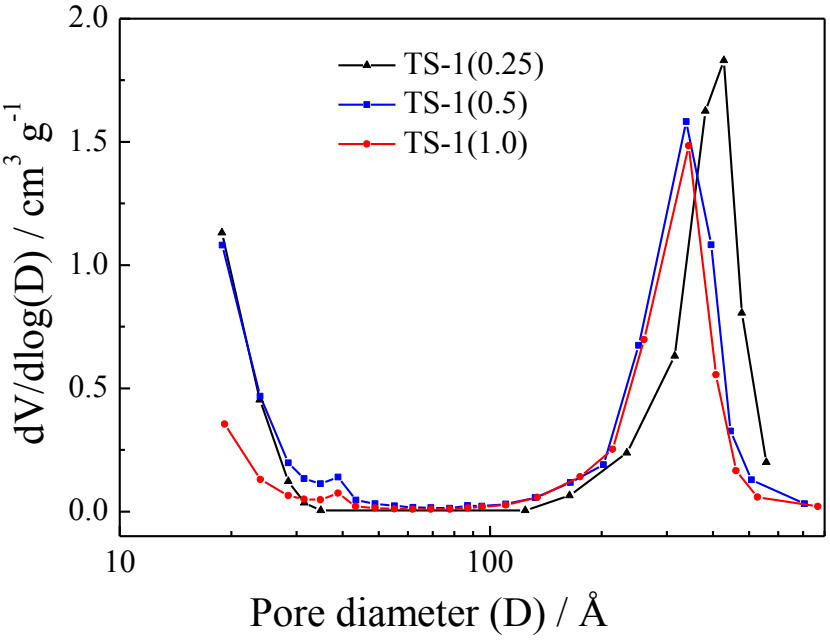

Figure 14: BJH pore size distributions of TS-1 beads.

Table 1 shows data for the Ti content, BET surface areas, micropore, mesopore and total pore volumes as well the external surface area of the three TS-1 samples. The Ti content increases with an increase in the Ti in the synthesis solution. It has been reported that the highest Ti content incorporated into the MFI-type structure was 2.5 Ti atoms / unit cell (2.8 mol-% Ti),[8] although the synthesis of TS-1 with a higher Ti content of up to 4.0 mol% has also been described.[19] Thus, whereas the large decrease in the surface area of TS-1(1.0) clearly indicates the presence of non-framework Ti, the high Ti content measured for TS-1(0.5) means that the presence of impurities of non-framework Ti in this sample is very likely. The increase in the mesopore volume and the external surface area for that sample, which is accompanied with a decrease in the micropore volume supports the possible presence of impurities of amorphous Si-Ti phases in TS-1(0.5).

The unusually high external surface areas of TS-1(0.25) and TS-1(0.5) could be explained by amorphous material present in the samples, which is confirmed by the corresponding XRD patters (Figure 7). The lower external surface area value measured for TS-1(1.0) can be explained by the formation of dense anatase as indicated by Raman analysis (Figure 8).

Table 1: Ti content and nitrogen adsorption data of the TS-1 beads.

Sample	Ti content (wt.%)	S_{BET} (m^2/g)	V_{μ} (cm^3/g)	V_{total} (cm^3/g)	V_{meso} (cm^3/g)	S_{EXT} (m^2/g)
TS-1(0.25)	1.1	724.8	0.10	0.67	0.57	506.0
TS-1(0.5)	3.1	671.4	0.07	0.73	0.66	507.8
TS-1(1.0)	6.9	352.4	0.07	0.50	0.43	195.7

3.2 PHOTOCATALYTIC EVALUATION

Photocatalytic evaluation of the beads was done using first order degradation kinetics of MB under UV irradiation. Figure 15 shows the effects of UV irradiation on MB in the presence of S-1 and TS-1 beads. In the presence of S-1, the MB solutions retained their distinctive blue colour after irradiation, which is evidence that Ti free samples had no photocatalytic activity.

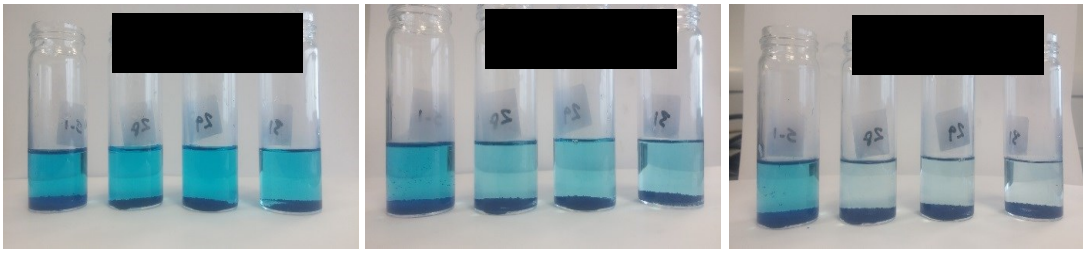

Figure 15: Photographs of MB solutions in the presence of TS-1 and S-1 beads, before and after UV irradiation. Left to right; S-1, TS-1(0.25), TS-1(0.5), TS-1(1.0).

Absorbance data from UV-Vis measurements of MB solutions before and after UV irradiation in the presence of TS-1 beads or CristalACTiV™ PC500 and without the presence of any photocatalysts are plotted below (Figure 16).

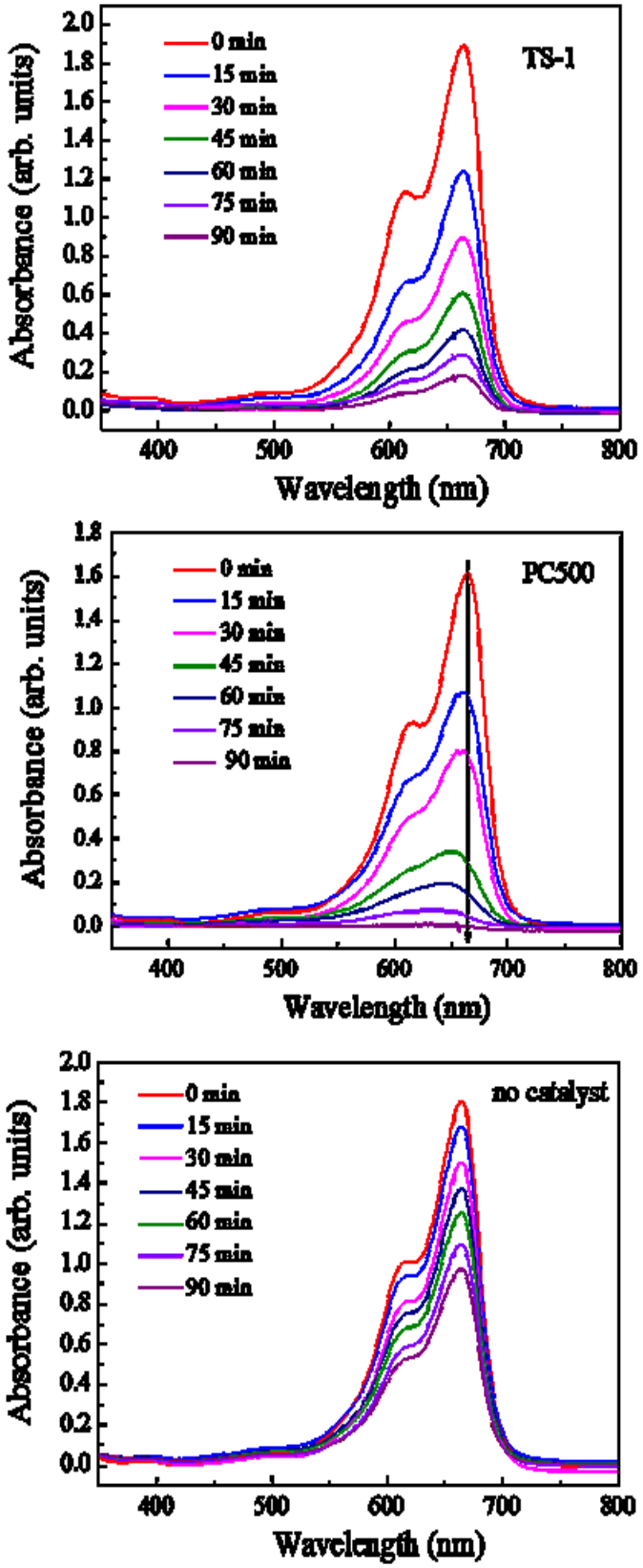

Figure 16: UV-Vis absorbance spectra for MB solutions before and after UV irradiation. From top to bottom: MB solutions in the presence of TS-1 (Representative), CristalACTiV™ PC500 and no catalyst.

The MB absorbance peak centred at 665 nm is arising from the hetero-polyaromatic linkage present in the dye. As can be seen in the case of CristalACTiV™ PC500, the peak at 665 nm experiences hypsochromic shift to lower wavelengths. This can be explained by N-demethylated degradation occurring concomitantly with the degradation of the phenothiazine functionality (Figure 17).[73]

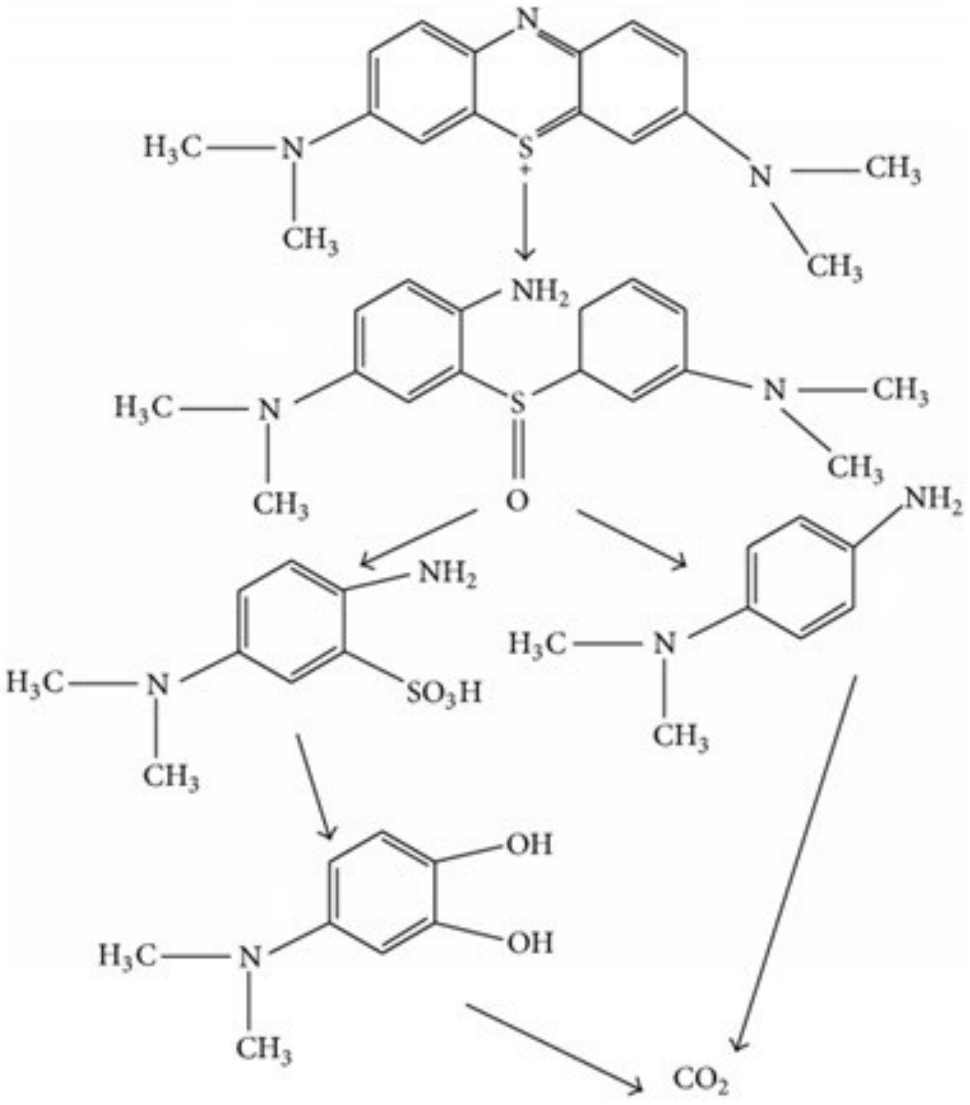

Figure 17: Degradation pathway of MB dye.[73]

Radicals from the photocatalyst, which is in direct coulombic interaction with the MB, cleave the bonds of the C–S^+=C functional group to C–S(=O)–C. This requires conservation of the double bond conjugation, inducing the opening of the central aromatic ring containing the S and N atoms. This shift is not observed for MB solutions in the presence of TS-1 beads or in the absence of a photocatalyst. The difference in the absorbance data could possibly be due the fine particle size of CristalACTiV™ PC500 causing aggregation of particles in solution caused by the absence of stirring, whereas the TS-1 beads are free flowing highly porous structures. It is possible aggregation of the PC500 leads to changes in the absorbance data due to a smaller surface area of the catalyst being available for photocatalytic degradation of the MB.

The first order rate constants of MB degradation in the presence or absence of photocatalysts was calculated by plotting a graph using $\ln\left(\frac{A}{A_0}\right) = -kt$, here A_0 is the absorbance at 665 nm after equilibrating and prior to UV irradiation, A is the corresponding absorbance at different irradiation times, and k is the first order rate constant. The equation used for the plots was derived from the first order rate equation as follows.

$$\text{Rate} = -\frac{dA}{dt} = kA$$

$$\frac{dA}{A} = -kdt$$

$$\int_{A_0}^{A} \frac{1}{A} dA = -\int_{t_0}^{t} kdt$$

$$\ln(A) - \ln(A_0) = -kt$$

$$\ln\left(\frac{A}{A_0}\right) = -kt$$

CristalACTiV™ PC 500 was found to be more active than TS-1 beads by a factor of 1.2 to 1.5 (Table 2). However, the TS-1 beads have the advantage of being easily separated from the MB solutions by decanting, without the need for high speed centrifugation like CristalACTiV™ PC500. Examining the rate constants (Table 2), there is no appreciable loss in the activity of the TS-1 beads in up to five cycles.

Table 2: First order rate constants of MB degradation under UV irradiation at 35 °C, with correlation coefficients, in the presence of TS-1 beads.

	First order rate constants (s^{-1}) (R^2)		
Cycle	**TS-1(0.25)**	**TS-1(0.5)**	**TS-1(1.0)**
1	4.24×10^{-4} (0.998)	4.60×10^{-4} (0.953)	4.55×10^{-4} (0.997)
2	4.92×10^{-4} (0.991)	5.16×10^{-4} (0.989)	5.01×10^{-4} (0.983)
3	4.80×10^{-4} (0.998)	4.46×10^{-4} (0.997)	4.12×10^{-4} (0.998)
4	4.81×10^{-4} (0.995)	4.96×10^{-4} (0.995)	4.63×10^{-4} (0.996)
5	5.11×10^{-4} (0.987)	4.95×10^{-4} (0.985)	4.72×10^{-4} (0.947)

Corresponding values for MB without catalyst and in the presence of CristalACTiV™ PC500 are 1.10×10^{-4} (0.991) and 6.13×10^{-4} (0.954) respectively.

Figure 18 shows a schematic diagram of the TS-1 beads and their cycle of usage. As can be seen, the TS-1 beads retain the vibrant blue colour of the MB even after the MB has degraded in solution. Desorption of the dye from the beads and back into solution was not observed and colour did not lessen upon further UV irradiation. This arises from attraction between the cationic dye and the negatively charged TS-1 lattice framework (The negatively charged lattice of TS-1 arises from the highly alkaline (pH > 6.7) synthesis

environment used, due to the zeta potential of TS-1),[27] this electrostatic effect effectively acts to capture and store the MB in the beads. As a consequence, the adsorption capacity of TS-1 beads for MB is reduced upon reuse. The initial adsorption capacity of the beads could be restored by calcining to remove the dye. However repeated calcining lead to structural changes, such as the formation of anatase. Irradiation of beads which had been soaked in MB and left to dry showed no change in colour upon UV irradiation; without the presence of water in the MB solutions, diffusion of MB and the subsequent degradation products to and from TS-1 active sites cannot occur.

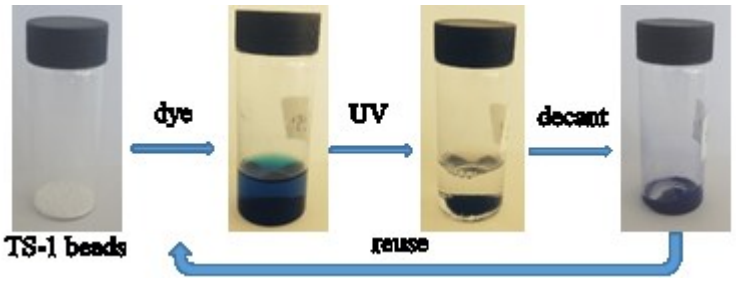

Figure 18: Schematic diagram of TS-1 beads and their cycle of use.

No substantial difference in the degradation rates of MB for TS-1 samples containing different amounts of Ti was observed. As shown by the XRD, Raman and gas adsorption data, as Ti content increases in a sample, TS-1 crystallinity and surface area decrease and the formation of anatase occurs. Anatase is well known to be the most photocatalytically active phase of TiO_2 materials. The formation of anatase appears to compensate for the lower surface area, along with preservation of the mesoporous structure of the beads. This leads to the similar activities measure between the different TS-1 samples. The inverse trend of the influence of Ti content and the surface area on the photocatalytic activity of TiO_2-SiO_2 beads prepared by resin templating has been discussed before.[70] Cani and Pescarmona stated that the lower activity of the mesoporous

beads, when compared to Degussa P25, could be explained by diffusion issues of the bulky MB molecule. However, previous studies of resin templating,[64,65,66] as well as the results presented in this study, show the variations in secondary porosity caused by resin removal are not great. This indicates that the active centres of TS-1 are responsible for the comparable rates of photocatalytic degradation of MB between TS-1 and CristalACTiV™ PC500.

Figure 18 shows the first order kinetic plots of MB degradation for monomers and dimers. The influences of TS-1 on degradation rate of MB monomers and dimers are equivalent. However, CristalACTiV™ PC500 shows higher degradation rates for the monomers than the dimers of MB. The porosity of the TS-1 may be facilitating accessibility of the monomers and dimers leading to coulombic interactions.

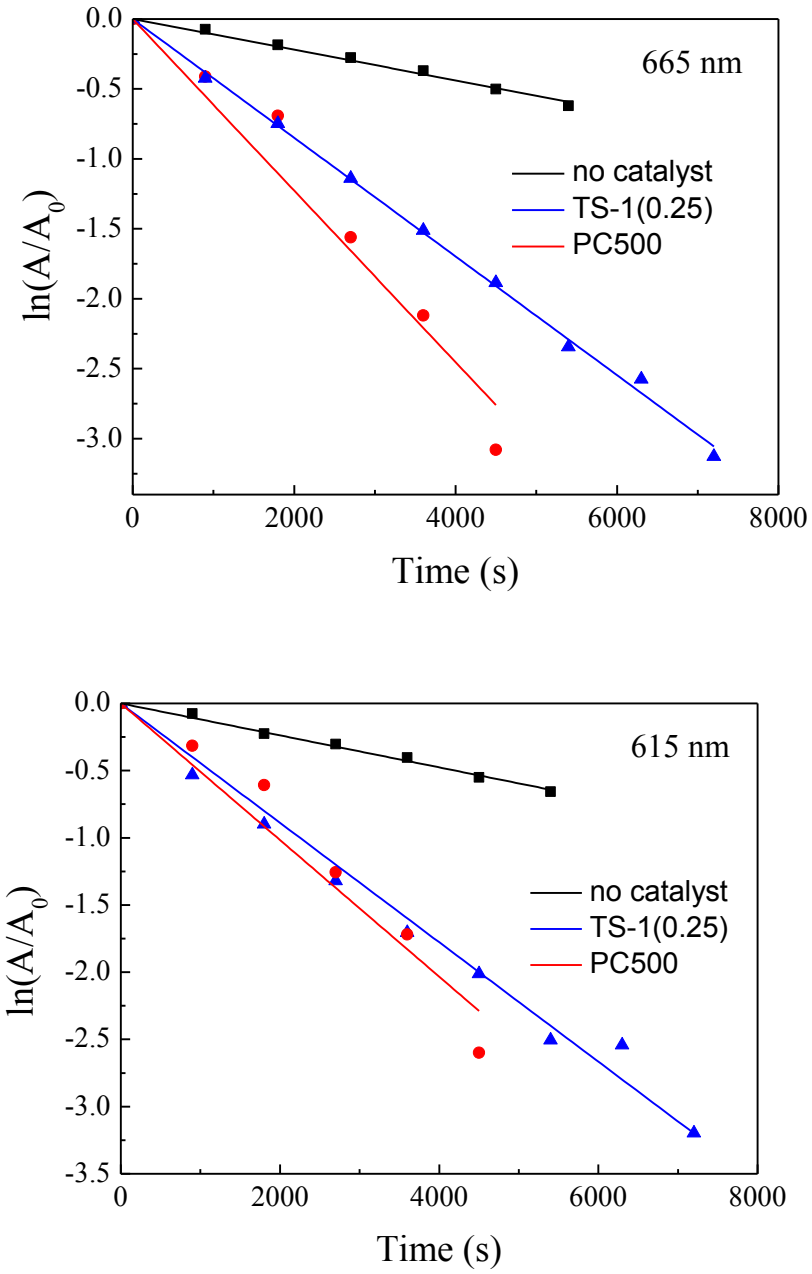

Figure 19: First order kinetic plots for the degradation of MB monomers (665 nm) and dimers (615 nm) in the absence of a photocatalyst and the presence of CristalACTiV™ PC500 or TS-1 beads.

Differences in rates between CristalACTiV™ PC500 and TS-1 suggest that dye binding sites are weaker in CristalACTiV™ PC500 than in TS-1, with preferential binding of dimers being shown.

Further evaluation of photocatalytic properties of TS-1 and CristalACTiV™PC500 were performed via BDS measurements. This real time method is able to probe excess charge carrier dynamics over extended periods and can correlate data with the surface reactions taking place. Large number of phonons (heat) act as mobile free carriers are generated, which reduces the ability of the microwave cavity to store power (attenuation of microwave power). The cavity stores power at certain frequencies due to the oscillating electric and magnetic fields of the microwave energy, which reach a maximum when they are resonant with the cavity. This separation of charge, in effect, reduces the dielectric constant and increases the conductivity of the material. Figure 20 shows that the temporal profiles of CristalACTiV™ PC500 and TS-1 are distinctly different. For CristalACTiV™PC500, the greater attenuation of power stored by the microwaves cavity suggests more free-carriers are produced in the high surface area anatase nanopowder. Power reaches a maximum quickly and levels off due to free carrier production being in competition with shallow-trapping at surface sites and recombination of carriers. When the light source is switched off after 1800 s, a rapid decrease in the attenuation of power is seen as the free-carriers recombine. For TS-1, the initial reduction in microwave is less pronounced than CristalACTiV™ PC500; this suggests that either fewer free-carriers are produced or the free-carriers more effectively recombine and/or become trapped. It has been previously shown that silica and alumina on the surface of TiO_2 can effectively trap free-carriers.[88] The zeolite silica framework or amorphous silica matrix may be causing trapping to occur, thereby reducing the number of free-carriers and therefore lowering photoactivity. The slower attenuation of power observed in TS-1 after removal of the light source, suggests that trapped carriers recombine slower than in CristalACTiV™ PC500.

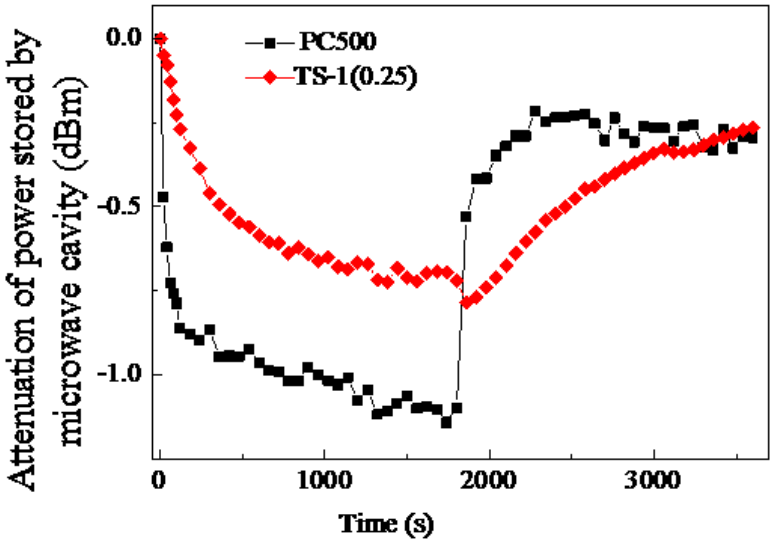

Figure 20: Attenuation of power, stored in microwave cavity with irradiation for 1800 s followed by removal of the light source, for CristalACTiV™ PC500 and TS-1.

4 CONCLUSIONS

In this study hierarchically porous TS-1 beads were synthesised using the resin templating method. Three samples of TS-1 beads were prepared with Ti contents of 1.1, 3.1 and 6.9 wt. %, respectively. The samples contained a large amount of amorphous material, which increased as Ti content increased. Formation of anatase lead to a drastic decrease in the surface area for the sample containing 6.9 wt. % Ti.

Photocatalytic activity of the TS-1 beads prepared were evaluated using first order kinetics of methylene blue (MB) decomposition under UV irradiation. Commercially available photocatalyst CristalACTiV™ PC500 was also evaluated and used as a reference material for comparison. Photocatalytic activity of CristalACTiV™ PC500 was higher than that for TS-1 beads by a factor of 1.2 to 1.5. However, the TS-1 beads have the advantage of being easily separable from solution by decanting, whereas CristalACTiV™ PC500 requires centrifugation at high speeds and as such results in loss of mass of photocatalyst and is energy and labour consuming. After each photocatalytic cycle, exhausted MB solutions were separated from TS-1 beads via decanting and replaced with fresh MB solutions. There was no appreciable loss in activity of TS-1 beads in up to five cycles of photocatalytic testing. All TS-1 samples prepared displayed similar activities, regardless of Ti content. The lower surface areas of TS-1 samples prepared with high Ti content were compensated for by the formation of highly photoactive anatase. Microwave resonance broadband dielectric loss (BDS) measurements showed that free-carrier production was higher in CristalACTiV™PC500 than TS-1, however in CristalACTiV™ PC500 these free-

carriers more effectively recombined upon removal of the light source. Further optimisation of TS-1 samples could reduce free-carrier trapping and thereby give comparable photoactivity to CristalACTiV™ PC500 with the extra advantage of easier reuse and recycling in photocatalytic reactions based in a liquid media.

5 FUTURE WORK

Possibilities for future work include further optimisation of TS-1 beads to circumvent free-carrier trapping, thereby improving photocatalytic activity. Incorporation of graphene into TS-1 has been shown to increase photocatalytic decomposition of dyes by up to a factor of 25. [89] Work on the hybridising of TS-1 beads with graphene is worth studying. Also worth exploring is the deposition of additional active phases, in order to produce TS-1 which is responsive to light in the visible spectrum. Research has shown that the addition of transition metal ions via doping, can improve the catalytic rates of materials produced and improve visible light sensitivity.[44]

Further work could also include determination of the photocatalytic activity of TS-1 for degradation of MB in the presence of H_2O_2. Another direction is to test TS-1 macrostructures for other photocatalytic reactions, for instance for reactions in a gas phase such as the photocatalytic breakdown of acetone to CO_2. Another aspect of potential study is the study of photocatalytic decomposition of larger and bulkier dyes, such as methyl orange, in the presence of TS-1 beads in order to assess the steric effects affecting active site accessibility. Another aspect warranting further study is the nature of the Ti sites found within the TS-1 beads, via UV-Vis spectroscopy. This would allow determination of the nature of the active sites used during photocatalytic processes.

Proper assessment of the mechanical properties of the beads also has potential for future research. Studying the effects of amorphous material in samples and synthesis times and temperatures in order to quantify the amount of stress the beads can withstand without disintegrating during use.

Although not necessary in the case of the TS-1 beads prepared in this body of work, a study of the effects of regeneration by calcination is another possibility for future work. Exposure to high temperatures when calcined may have an unwanted effect on the active sites and mechanical properties of the TS-1 beads. Thermogravimetric analysis could also be applied in order to characterise the lowest possible temperature required for catalyst regeneration.

6 REFERENCES

1. R. M. Barrer, *Zeolites and Clay Minerals as Sorbents and Molecular Sieves*, Academic Press, London, 1978.

2. W. M. Meier, D. H. Olson and C. Baerlocher, *Zeolites*, 1996, **17**, 1–229.

3. Q. Li, *Colloidal Zeolites from Nucleation to Zoned Films by Seeded Growth*, PhD thesis, Luleå University of Technology, 2004, 1-3.

4. Z. Weng, *Molecular Sieve Films and Zoned Materials*, PhD thesis, Luleå University of Technology, 2003, 1-7.

5. M. E. Davis, *Nature*, 2002, **417**, 813-821.

6. S. Mintova, M. Jaber and V. Valtchev, *Chem. Soc. Rev.*, 2015, Advance Article.

7. L. Tosheva and V. Valtchev, *C. R. Chimie*, 2005, **8**, 475-484.

8. U.S. Patent 4410501, 1983.

9. International Zeolite Association, http://www.iza-structure.org/databases (accessed July 2015).

10. G. Bellussi and V. Fattore*, Stud. Surf. Sci. Catal.,* 1991, **69**, 79-92.

11. D. R. C. Huybrechts, L. De Bruycker and P. Jacobs, *Nature*, 1990, **345**, 240.

12. M. G. Clerici and P. Ingallina, *J. Catal*., 1993, **140**, 71-83.

13. B. Kraushaar and J. H. C. van Hooff, *Catal. Lett*., 1989, **2**, 43.

14. US Patent 4480135, 1984.

15. A. J. H. P. van der Pol and J. H. C. van Hooff, *Appl. Catal*., 1993, **106**, 97.

16. T. Tatsumi, M. Nakamura, S. Negishi and H. Tominaga, *J. Chem. Soc., Chem. Commun*., 1990, 476.

17. B. Notari, *Catal. Today*, 1993, **18**, 163-17.

18. D.R.C. Huybrechts, P.L. Buskens and P.A. Jacobs, *J. Mol. Cat*., 1992, **71**, 129.

19. A. J. H. P. Van Der Pol and J. H. C. Van Hooff, *Appl. Catal. A.*, 1992, **92**, 93.

20. A. Thangaraj, M. J . Eapen, S . Sivasanker and P . Ratnasamy, *Zeolites*, 1992, **12**, 943.

21. A. Tuel and Y. Ben Taarit, *Zeolites*, 1994, **14**, 272.

22. G. Bellussi, A. Carati, M. G. Clerici and A. Esposito, *Proc. of 5th Symp. on Scient*., Louvain-la-Neuve, 1990, Preprints, 201.

23. D. P. Serrano, R. Sanz, P. Pizarro, I. Moreno and S. Medina, *Appl. Catal. B.*, 2014, **146**, 35-42.

24. D. P. Serrano, R. Sanz, P. Pizarro, I. Moreno and S. Shami, *Microporous Mesoporous Mater.*, 2014, **189**, 71-82.

25. K. Lin, O. I. Lebedev, G. van Tendeloo, P. A. Jacobs and P. P. Pescarmona, *Chem. Eur. J.*, 2010, **16**, 13509-13518.

26. L. Tosheva and V. Valtchev, *Chem. Mater.*, 2005, **17**,2494-2513.

27. G. Zhang, J. Sterte and B. Schoeman, *Chem. Mater*., 1997, **9**, 210-217.

28. D. P. Serrano, M. A. Uguina, G. Ovejero, R. Van Grieken and M. Camacho, *Chem. Commun.*, 1996, 1097.

29. M. A. Uguina, D. P. Serrano, G. Ovejero, R. Van Grieken and M. Camacho*, Appl. Catal. A.,* 1995, **124**, 391-408.

30. I. Schmidt, A. Krogh, K. Wienberg, A. Carlsson, M. Brorson and C. J. H. Jacobsen, *Chem. Commun*., 2000, 2157-2158.

31. Z. Wang, L. Xu, J. Jiang, Y. Liu, M. He and P. Wu, *Microporous Mesoporous Mater.*, 2012, **156**, 106-114.

32. Q. Lv, G. Li and H. Sun, *Fuel*, 2014, **130**, 70-75.

33. G. D. Lee, S. K. Jung, Y. J. Jeong, J. H. Park, K. T. Lim, B. H. Ahn and S. S. Hong, *Appl. Catal. A*., 2003, **239**, 197–208.

34. Z. Juan, Z. Dishun, Y. Liyan and L. Yongbo, *Chem. Eng. J.*, 2010, **156**, 528–531.

35. T. Ban, S. Kondoh, Y. Ohya and Y. Takahashi, *Phys. Chem. Chem. Phys.,* 1999, **1**, 5745-5752.

36. A. Corma and H. Garcia*, Chem. Commun*., 2004, 1443-1459.

37. S. A. Yuan, W. H. Chen and S. S. Hu, *Mater. Sci. Eng. C*., 2005, **25**, 479.

38. J. H. Braun, A. Baidins and R. E. Marganski, *Prog. Org. Coat*., 1992, **20**, 105.

39. A. Fujishima and K. Honda, *Nature*, 1972, **37**, 238.

40. O. Carp, C. L. Huisman and A. Reller, *Prog. Solid State Ch.*, 2004, **32**, 33-177.

41. A. L. Linsbigler, G. Q. Lu and J. T. Yates Jr., *Chem Rev*, 1995, **95**, 735.

42. K. Tanaka, M. F. V Capule, T. Hisanaga, *Chem. Phys. Lett.*, 1991, **187**, 73.

43. A. P. Alivisatos, *J. Phys. Chem*. 1996, **100**, 13226.

44. J. Schneider, M. Matsuoka, M. Takeuchi, J. Zhang and Y. Horiuchi, *Chem. Rev*., 2014, **114**, 9919−9986.

45. X. Chen and S. Mao, *Chem. Rev*. 2007**, 107**, 2891-2959.

46. Q. Zhang and L. Gao, *Langmuir*, 2003, **19**, 967.

47. A. B. Corradi, F. Bondioli, B. Focher, A. M. Ferrari, C. Grippo, E. Mariani and C. Villa, *J. Am. Ceram. Soc.* 2005, **88**, 2639.

48. X. Wu, Q. Z. Jiang, Z. F. Ma, M. Fu and W. F. Shangguan, Solid *State Commun.* 2005, **136**, 513.

49. D. Chen, L. Cao, F. Huang, P. Imperia, Y. B. Cheng and R. Caruso*, J. Am. Chem. Soc.*, 2005, **132**, 4438-4444.

50. D. Chen, L. Cao, D. Chen and R. Caruso, *Appl. Mater. Int*., 2013, **5**, 9421-9428.

51. J. C. Yu, L. Zhang and J. Yu, *New J. Chem*. 2002, **26**, 416.

52. Y. Zhuang, H. Y. Song, G. Li and Y. Xu, *J. Mater. Lett*. 2010, **64**, 2491.

53. J. C. Yu, X. Wang, L. Wu, W. Ho, L. Zhang and G. Zhou, *Adv. Funct. Mater.*, 2004, **14**, 1178.

54. M. H. Bartl, S. P. Puls, J. Tang, H. C. Lichtenegger and G. D. Stucky, *Angew. Chem., Int. Ed.* 2004, **43**, 3037.

55. J. C. Yu, L. Zhang and J. Yu, *J. Chem. Mater.* 2002, **14**, 4647.

56. P. D. Cozzoli, R. Comparelli, E. Fanizza, M. L. Curri and A. Agostiano, *Mater. Sci. Eng. C*., 2003, **23**, 707.

57. S. Y. Chae, M. K. Park, S. K. Lee, T. Y. Kim, S. K. Kim and W. I. Lee, *Chem. Mater.* 2003, **15**, 3326.

58. Y. Bessekhouad, D. Robert, J. V. Weber, N. Chaoui, *J. Photochem. Photobiol. A*., 2004, **167**, 49.

59. J. Schneider, M. Matsuoka, M. Takeuchi, J. Zhang and Y. Horiuchi, *Chem. Rev*., 2014, **114**, 9919−9986.

60. N. N. Yan, Z. Q. Zhu, J. Zhang, Z. Y. Zhao and Q. J. Liu, *Mater. Res. Bull.* 2012, **47**, 1869.

61. J. F. Zhu, W. Zheng, H. E Bin, J. L. Zhang and M. Anpo, *J. Mol. Catal. A: Chem*., 2004, **216**, 35.

62. C. C. Wang, Z. Zhang and J. Y. Ying, *Nanostruct. Mater*., 1997, **9**, 583.

63. Z. Zhang, C. C. Wang, R. Zakaria and J. Y. Ying, *J. Phys. Chem. B.*, 1998, **102**, 10871.

64. L. Tosheva, V. Valtchev and J. Sterte, *Micropor. Mesopor. Mat*., 2000, **35**-**36**, 621-629.

65. L. Tosheva, B. Mihailova, V. Valtchev and J. Sterte, *Micropor. Mesopor. Mat*., 2001, **48**, 31-37.

66. L. Tosheva and J. Sterte, *Stud. Surf. Sci. Catal*., 2002, **142**, 183-190.

67. L. Tosheva, *Molecular Sieve Macrostructures Prepared by Resin Templating*, PhD thesis, Luleå University of Technology, 2001, 18-30.

68. S. Zhang, Y. Jiang, S. Li, X. Xu and K. Lin, *App. Catal. A.*, 2015, **490**, 57-64.

69. K. Lin, O. I. Lebedev, G. Van Tendeloo, P. A. Jacobs and P. P. Pescarmona, *Chem. Eur. J.*, 2010, **16**, 13509-13518.

70. D. Cani and P. Pescarmona, *J. Catal*., 2014, **311**, 404-411.

71. S. J. Greeg, K. S. W. Sing, Adsorption, Surface Area and Porosity, 2nd Edition, Academic Press, London, 1982.

72. J. Weber and V. C. Stickney, *Wat. Res*., 1993, **27**, 63.

73. A. Houas, H. Lachheb, M. Ksibi, E. Elaloui, C. Guillard and J. M. Hermann*, Appl. Catal. B: Environ*, 2001, **31**, 145.

74. A. Ajmal, I. Majeed, R. N. Malik, H. Idriss and M. A. Nadeem, *RSC. Adv*., 2014, **4**, 37003-37026.

75. I. K. Konstantinou and T. A. Albanis, *Appl. Catal. B: Environ*., 2004, **49**, 1-14.

76. M. N. Chong, B. Jin, C. W. K. Chow and C. Saint, *Wat. Res.*, 2010, **44**, 2997-3027.

77. A. Ajmal, I. Majeed, R. N. Malik, H. Idriss and M. A. Nadeem*, RSC Adv.,* 2014, **4**, 37003-37026.

78. T. C. Jagadale, S. P. Takale, R. S. Sonawane, H. M. Joshi, S. I. Patil, B. B. Kale and S. B. Ogale, *J. Phys. Chem. C* 2008, **112**, 14595.

79. I. Justicia, P. Ordejón, G. Canto, J. L. Mozos, J. Fraxedas, G. A. Battiston, R. Gerbasi and A. Figueras, *Adv. Mater*. 2002, **14**, 1399.

80. M. Xing, J. Zhang and F. Chen, *J. Phys. Chem. C* 2009, **113**, 12848.

81. O. Yazdani, M. Irandoust, J. B. Ghasemi and Sh. Hooshmand, *Dyes Pigments*, 2012, **92**, 1031-1041.

82. H. A. Le, L. T. Linh, S. Chin, and J. Jurng, *Powder Technology*, 2012, **225**, 167–175.

83. L. Tosheva, B. Mihailova, V. Valtchev and J. Sterte, *Micropor. Mesopor. Mat.*, 2000, **39**, 91-101.

84. Y. G. Li, Y. M. Lee and J. F. Porter; *J. Mat. Sci*., 2002, **37**, 1959-1965.

85. N. Mahdjoub, N, Allen, P. Kelly and V. Vishnyakov, *J. Photoch. Photobio. A*., 2010, **211**, 59-64.

86. E. Duprey, P. Beaunier, M. A. Springuel-Huet, F. Bozon-Verduraz, J. Fraissard, J. M. Manoli and J. M. Bregeault, *J. Catal.*, 1997, **165**, 22.

87. G. Bellussi, A. Carati, M. G. Clerici, G. Maddinelli and R. Millini, *J. Catal.*, 1992, **133**, 220-230.

88. N. S. Allen, M. Edge, A. Ortega, G. Sandoval, C. M. Liauw, J. Verran, J. Stratton and R. B. McIntyre, Polym. *Degrad. Stabil.*, 2004, **85**, 927-946.

89. Z. Ren, E. Kim, S. W. Pattinson, K. S. Subrahmanyam, C. N. R. Rao, A. K. Cheetham and D. Eder, *Chem. Sci*., 2012, **3**, 209-216.

89. C. Xu, G. P. Rangaiah and X. S. Zhao, *Ind. Eng. Chem. Res.*, 2014, **53**, 14641-14649.

90. Z. Zainal, C. S. Keng and A. H. Abdullah, *Malays. J. Anal. Sci.*, 2008, **12**, 111-117.

91. F. B. Li and X. Z. Li, *Chemosphere*, 2002, **48**, 1103-1111.

92. X. Z. Li, F. B. Li, C. L. Yang and W. K. Ge, *J. Photochem. Photobiol. A.,* 2001, **141**, 209-217.

93.

7 APPENDIX 1

This appendix lists the conference presentations and journal publications that were achieved as a result of this body of work.

1. TS-1 macrostructures for use in photocatalytic removal of organic pollutants from aqueous medium, oral presentation, 38th BZA Annual Conference.
2. S. P. D. Ormond, M. Ratova, P. Kelly, M. Edge, B. Mihailova and L. Tosheva, Titanium silicalite-1 macrostructures for photocatalytic removal of organic pollutants from aqueous media, submitted to Appl. Catal. B.

8 APPENDIX 2

This appendix contains supplementary graphs and tables to accompany the results found in this body of work.

Literature Rate Constant Summary Table

This table summarises the experimental conditions and rate constants, measured via first order decomposition kinetics of MB dye in the presence of TiO_2 based photocatalysts, that can be found in the literature.

Photocatalyst	Experimental Conditions	Rate Constant (s^{-1})	Reference
Mesoporous titania beads	3.125 g of photocatalyst, 160 ml of 1.56 ×10^{-5} M MB, Temp: 20 ± 1 °C, light source: Oriel 500 W (Xe)(200 - 380 nm).	5.50 ×10^{-4} to 7.83 ×10^{-4}	50
Degussa P25	0.01 to 0.025 g of photocatalyst, 50 ml of 6.25 ×10^{-5} to 1.09 ×10^{-4} M MB, light source: 350 W (Xe)(850 nm), 300 to 500 W (Hg)(365 nm).	7.83 ×10^{-4} to 1.92 ×10^{-3}	89
TiO_2 loaded activated carbon	0.5 to 2.0 g of photocatalyst, 15 ml of 6.25 ×10^{-4} M MB, Temp: 28 °C, light source: UV.	6.70 ×10^{-4} to 8.12 ×10^{-4}	90
Pt-TiO_2 nanopowder	0.2 g of photocatalyst, 165 ml of 4.69 ×10^{-5} M MB, light source: 110 W (Hg or Na)(365 - 420 nm).	1.05 ×10^{-3} to 1.74 ×10^{-3}	91
3% WO_x-TiO_2 powder	0.2 g of photocatalyst, 165 ml of 3.91 ×10^{-5} M MB, light source: 110 W (Na)(400-800 nm)	1.76 ×10^{-3}	92

ZSM-5 Reference XRD Pattern

Plotted below is an idealised reference XRD pattern for a 100 % crystalline ZSM-5 sample.[9] This is to allow comparison with TS-1 XRD patterns, which has the same MFI-type lattice structure as ZSM-5.

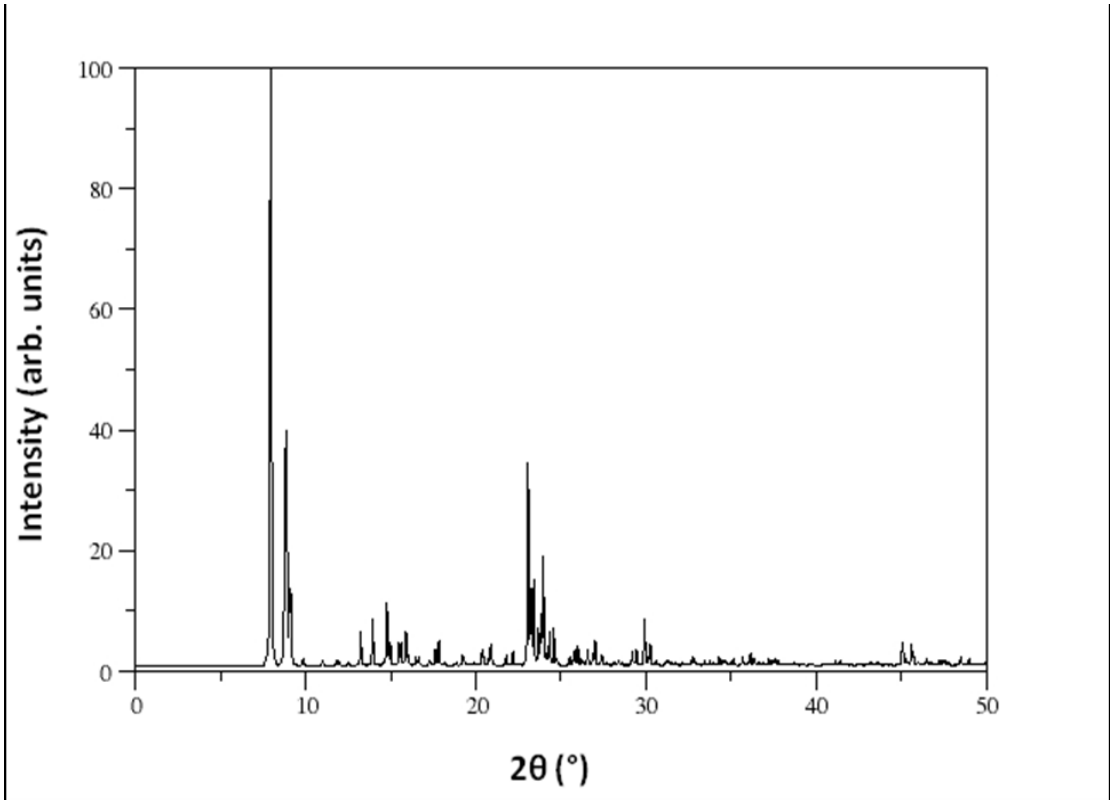

Absorbance vs wavelength plots

Below are the absorbance vs wavelength graphs plotted from the UV-Vis data gathered from each photocatalytic testing cycle of the TS-1 samples.

TS-1(0.25)

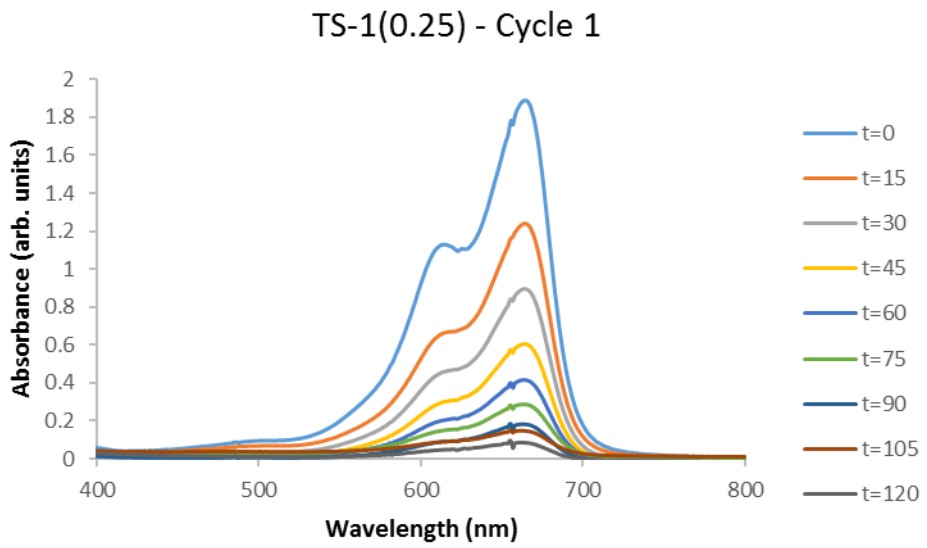
TS-1(0.25) - Cycle 1
Absorbance (arb. units)
Wavelength (nm)
t=0
t=15
t=30
t=45
t=60
t=75
t=90
t=105
t=120

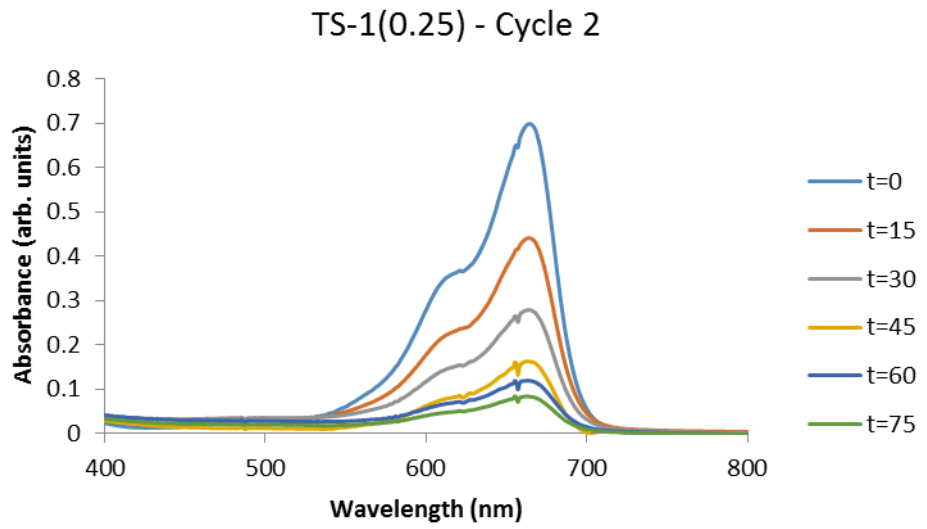
TS-1(0.25) - Cycle 2
Absorbance (arb. units)
Wavelength (nm)
t=0
t=15
t=30
t=45
t=60
t=75

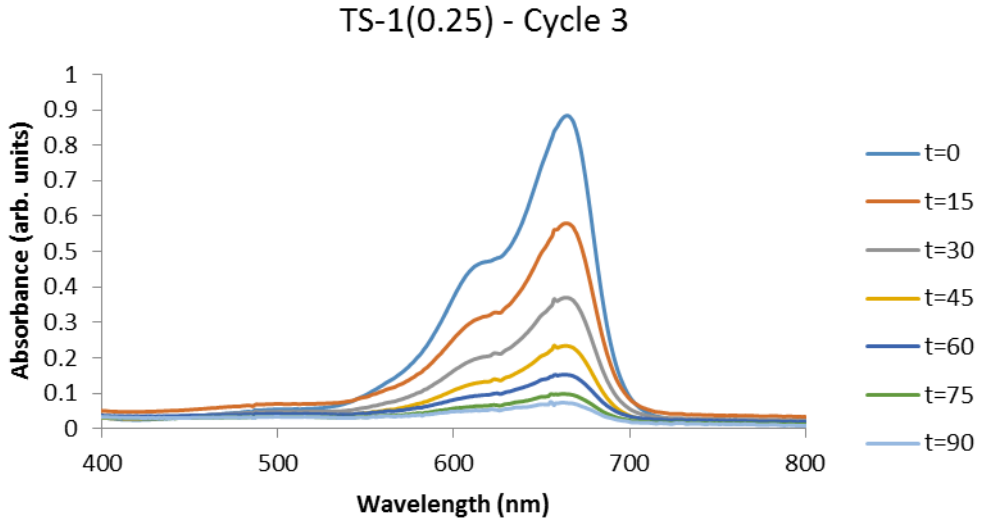
TS-1(0.25) - Cycle 3
Absorbance (arb. units)
Wavelength (nm)
t=0
t=15
t=30
t=45
t=60
t=75
t=90

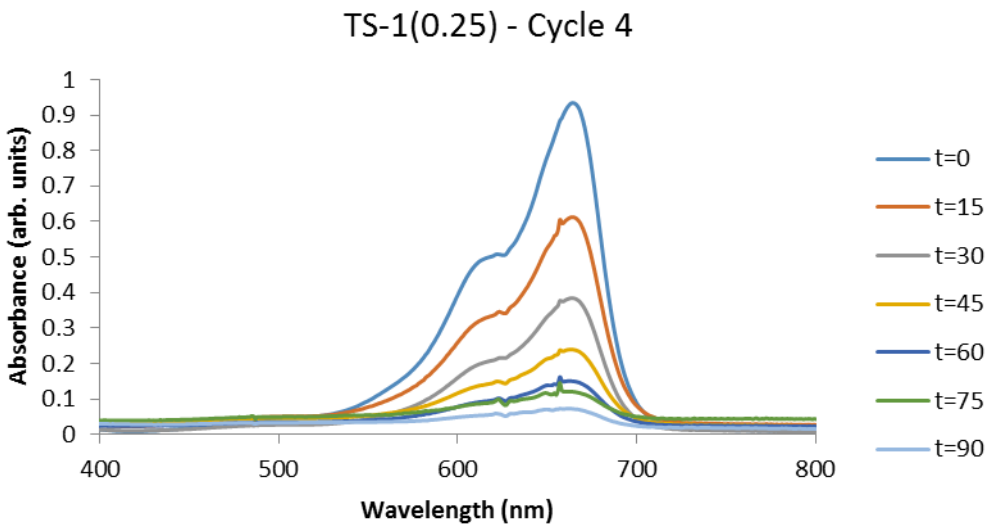
TS-1(0.25) - Cycle 4
Absorbance (arb. units)
1
0.9
0.8
0.7
0.6
0.5
0.4
0.3
0.2
0.1
0
400
500
600
700
800
Wavelength (nm)
t=0
t=15
t=30
t=45
t=60
t=75
t=90

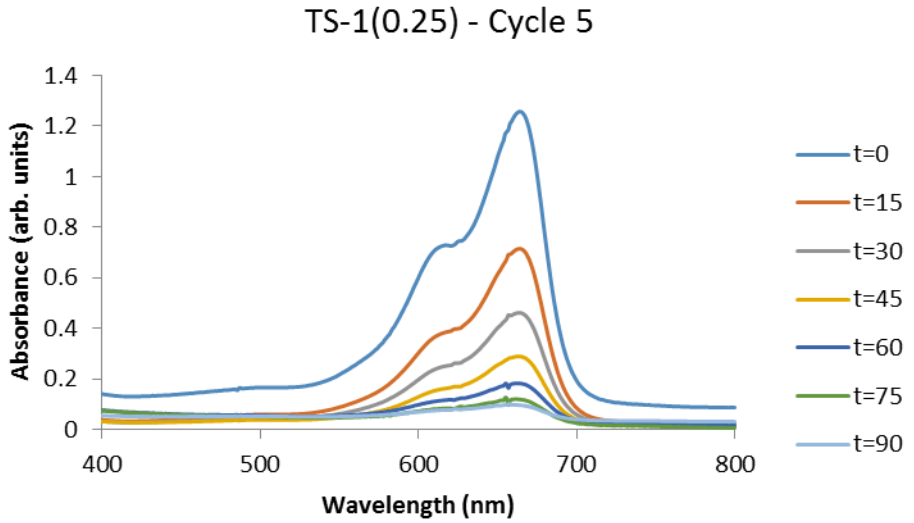
TS-1(0.25) - Cycle 5
Absorbance (arb. units)
1.4
1.2
1
0.8
0.6
0.4
0.2
0
400
500
600
700
800
Wavelength (nm)
t=0
t=15
t=30
t=45
t=60
t=75
t=90

TS-1(0.5)

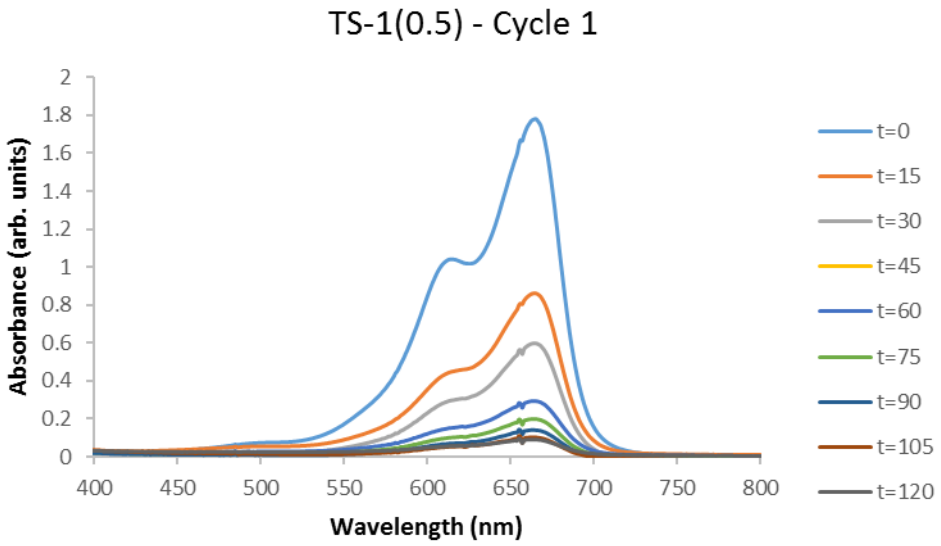
TS-1(0.5) - Cycle 1
Absorbance (arb. units)
Wavelength (nm)
t=0
t=15
t=30
t=45
t=60
t=75
t=90
t=105
t=120

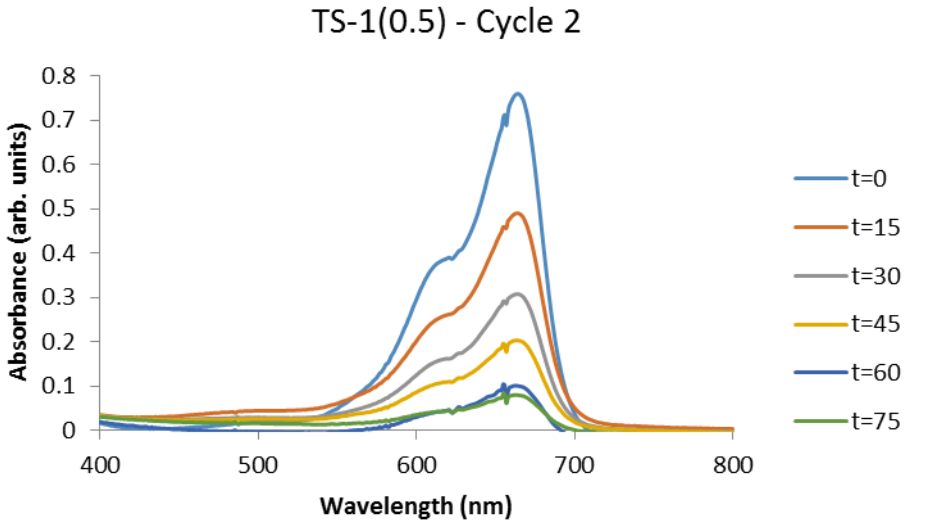
TS-1(0.5) - Cycle 2
Absorbance (arb. units)
Wavelength (nm)
t=0
t=15
t=30
t=45
t=60
t=75

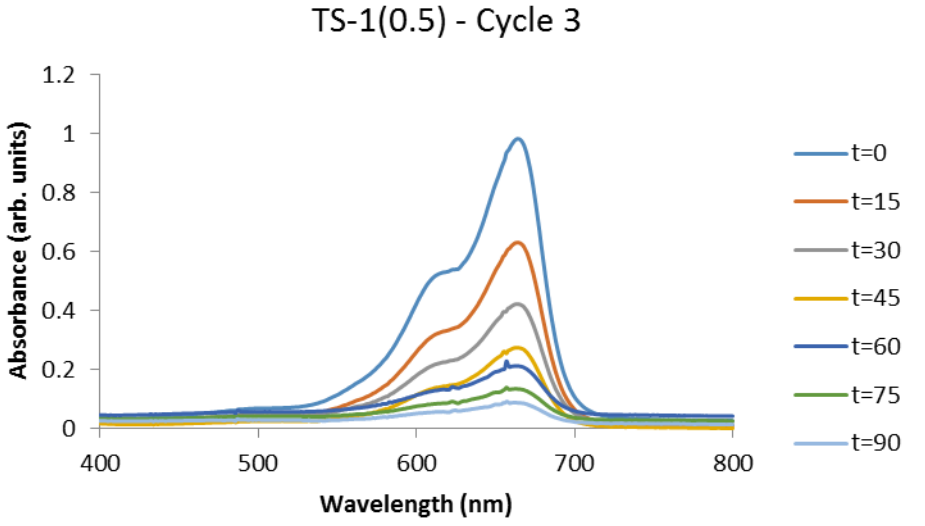
TS-1(0.5) - Cycle 3
Absorbance (arb. units)
Wavelength (nm)
t=0
t=15
t=30
t=45
t=60
t=75
t=90

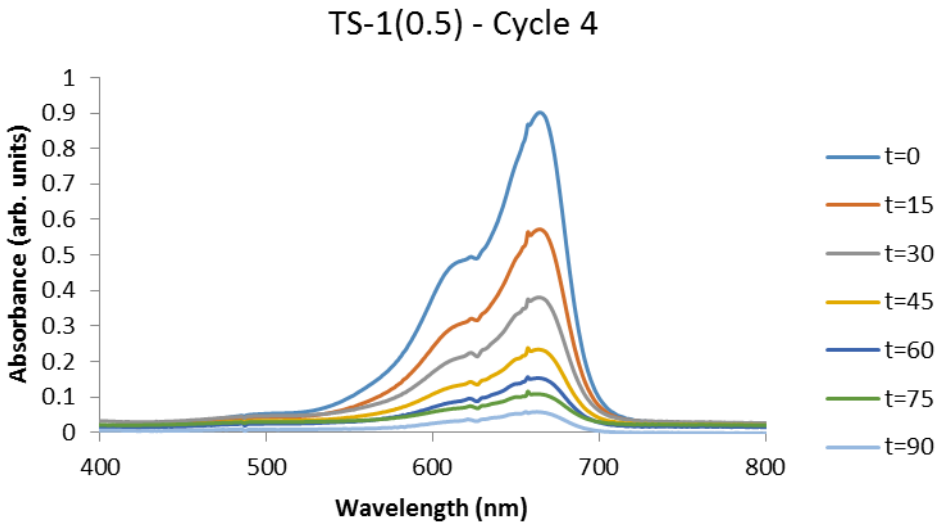
TS-1(0.5) - Cycle 4
Absorbance (arb. units)
1
0.9
0.8
0.7
0.6
0.5
0.4
0.3
0.2
0.1
0
400
500
600
700
800
Wavelength (nm)
t=0
t=15
t=30
t=45
t=60
t=75
t=90

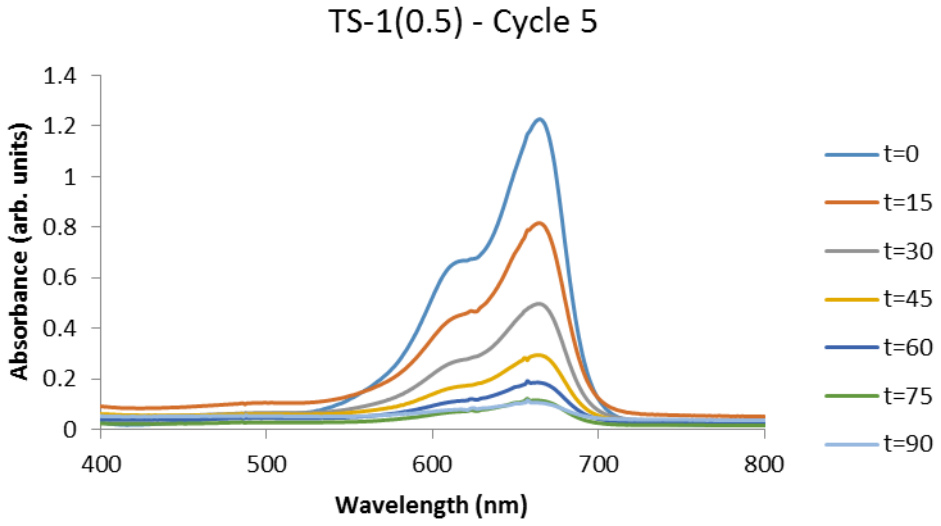
TS-1(0.5) - Cycle 5
Absorbance (arb. units)
1.4
1.2
1
0.8
0.6
0.4
0.2
0
400
500
600
700
800
Wavelength (nm)
t=0
t=15
t=30
t=45
t=60
t=75
t=90

TS-1(1.0)

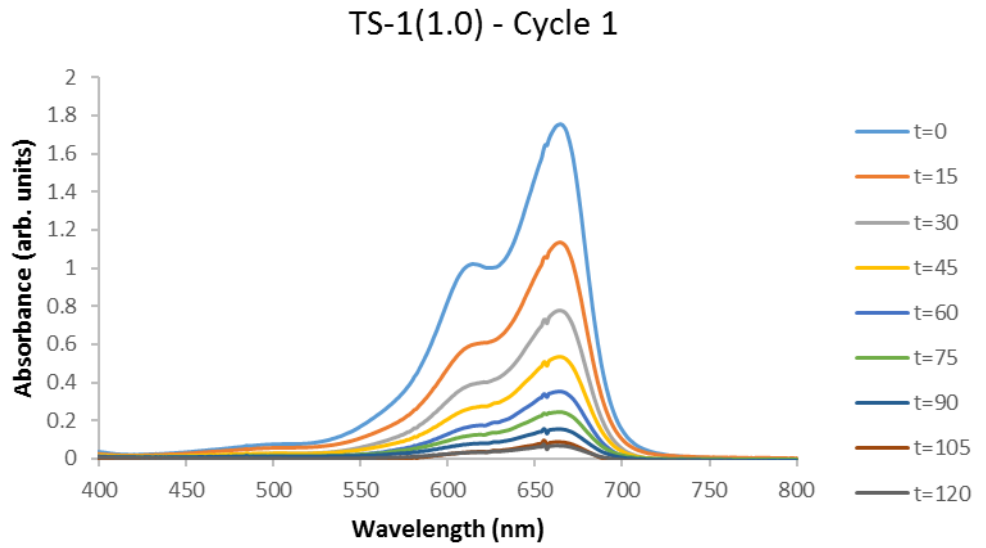
TS-1(1.0) - Cycle 1
Absorbance (arb. units)
Wavelength (nm)
t=0
t=15
t=30
t=45
t=60
t=75
t=90
t=105
t=120

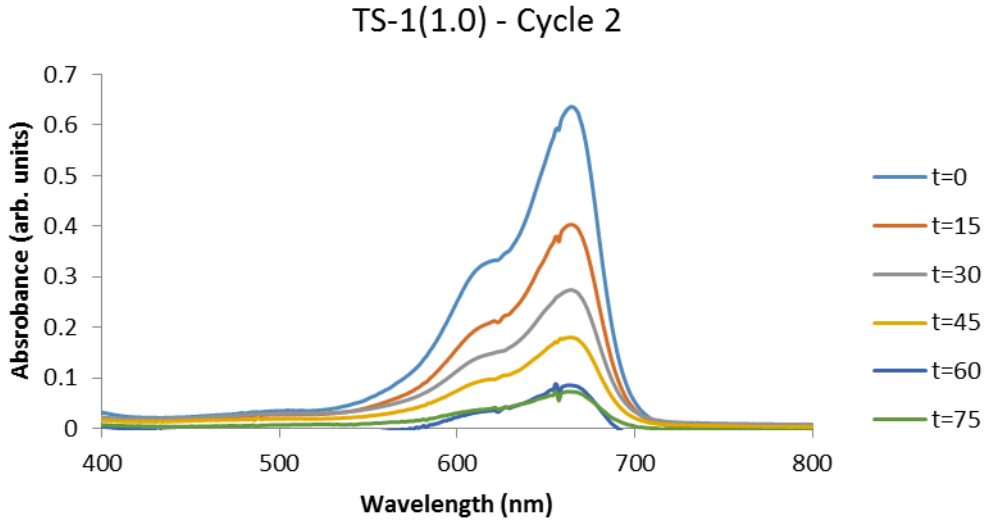
TS-1(1.0) - Cycle 2
Absrobance (arb. units)
Wavelength (nm)
t=0
t=15
t=30
t=45
t=60
t=75

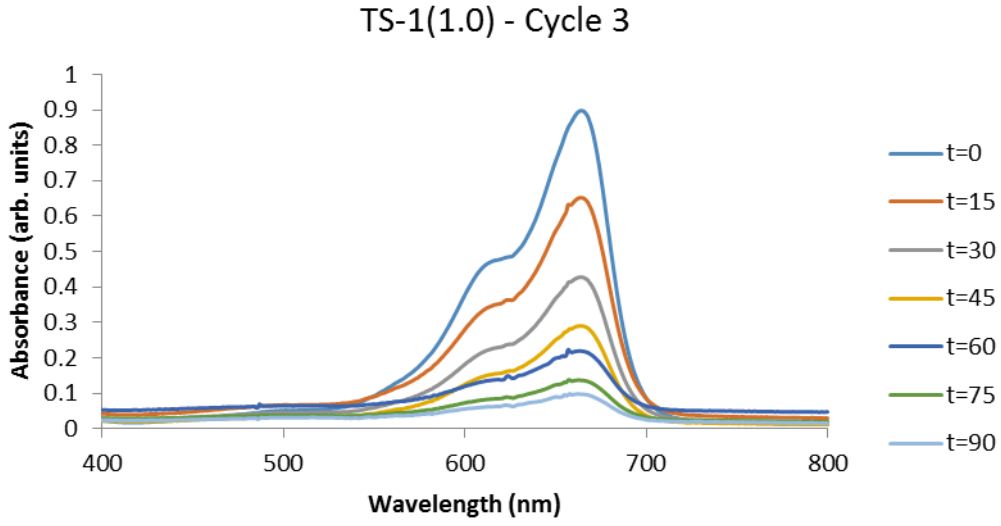
TS-1(1.0) - Cycle 3
Absorbance (arb. units)
Wavelength (nm)
t=0
t=15
t=30
t=45
t=60
t=75
t=90

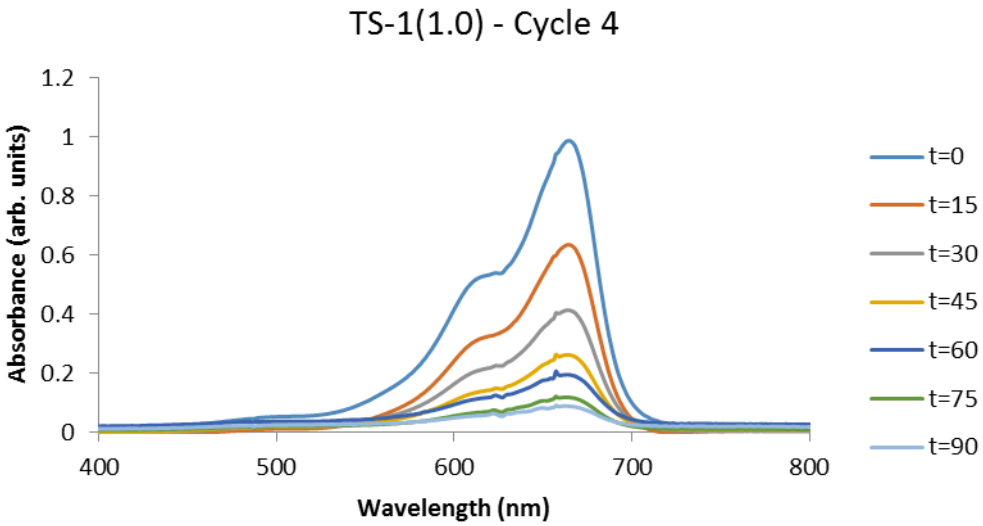

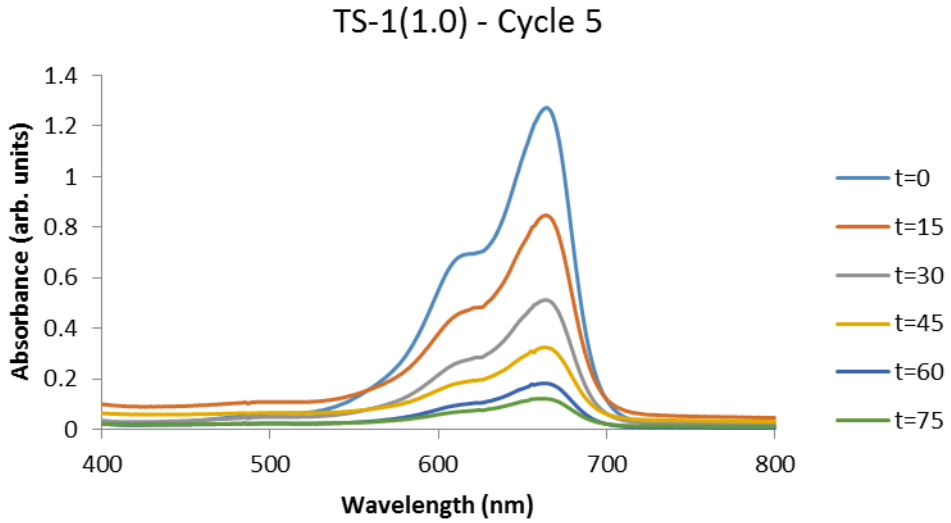

Absorbance vs time

Below are the absorbance vs time plots of degradation of MB in the presence of TS-1 beads. These graphs were used to calculate the first order rate constants found in Table 2. For clarity, the trend lines have been omitted.

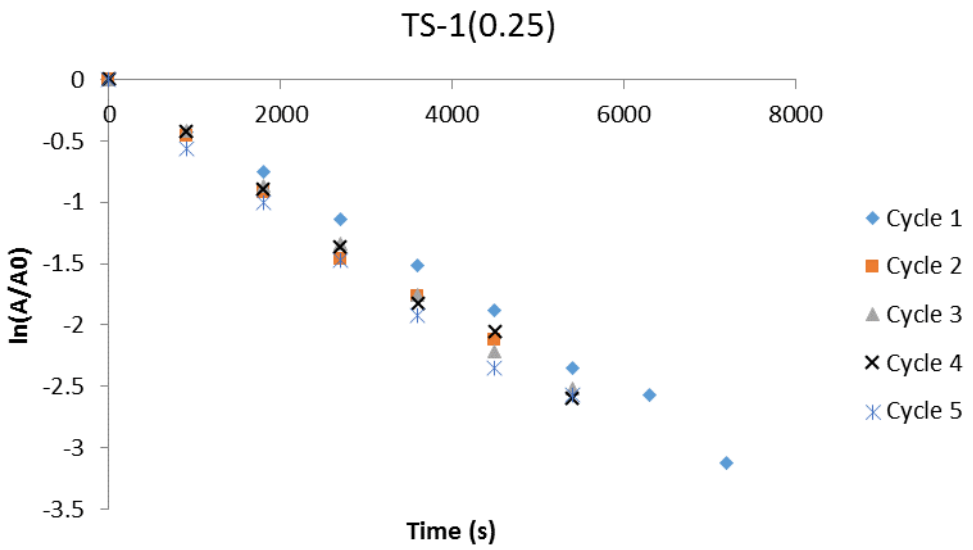
TS-1(0.25)
0
-0.5
-1
-1.5
-2
-2.5
-3
-3.5
0
2000
4000
6000
8000
ln(A/A0)
Time (s)
Cycle 1
Cycle 2
Cycle 3
Cycle 4
Cycle 5

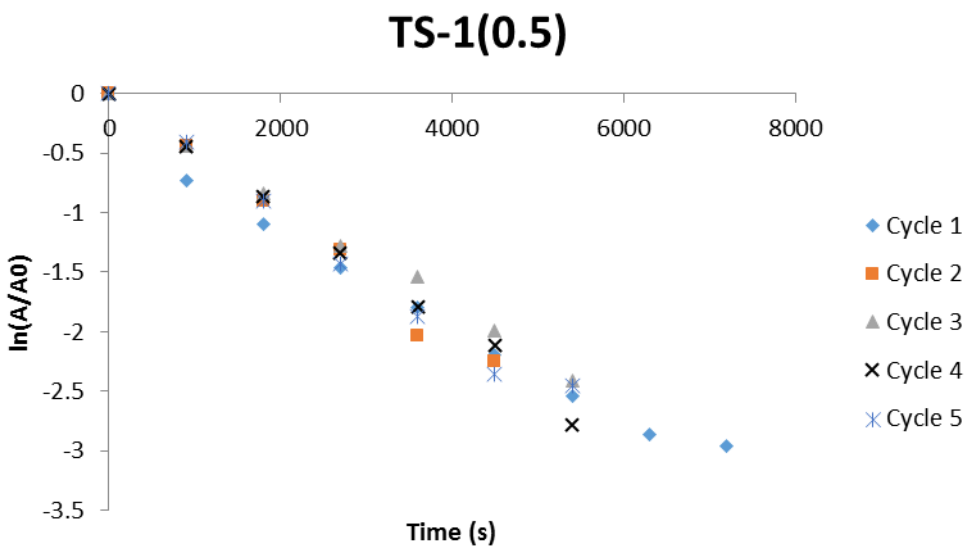
TS-1(0.5)
0
-0.5
-1
-1.5
-2
-2.5
-3
-3.5
0
2000
4000
6000
8000
ln(A/A0)
Time (s)
Cycle 1
Cycle 2
Cycle 3
Cycle 4
Cycle 5

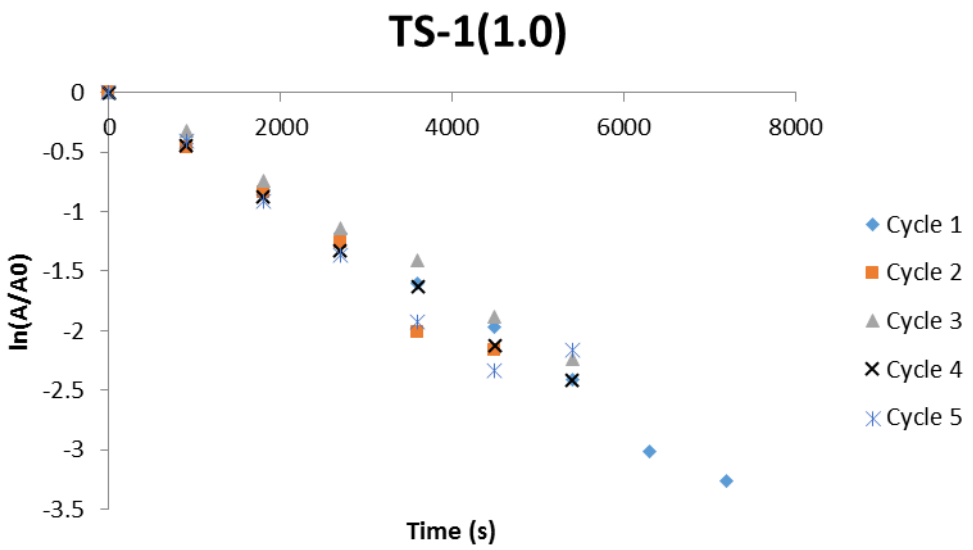
TS-1(1.0)
0
-0.5
-1
-1.5
-2
-2.5
-3
-3.5
0
2000
4000
6000
8000
ln(A/A0)
Time (s)
Cycle 1
Cycle 2
Cycle 3
Cycle 4
Cycle 5